

REPORT DOCUMENTATION PAGE

Form Approved
OMB NO. 0704-0188

Public Reporting burden for this collection of information is estimated to average 1 hour per response, including the time for reviewing instructions, searching existing data sources, gathering and maintaining the data needed, and completing and reviewing the collection of information. Send comment regarding this burden estimates or any other aspect of this collection of information, including suggestions for reducing this burden, to Washington Headquarters Services, Directorate for information Operations and Reports, 1215 Jefferson Davis Highway, Suite 1204, Arlington, VA 22202-4302, and to the Office of Management and Budget, Paperwork Reduction Project (0704-0188,) Washington, DC 20503.

1. AGENCY USE ONLY (Leave Blank)

2. REPORT DATE
12/02

3. REPORT TYPE AND DATES COVERED
Final Technical Report 5/99-11/02

4. TITLE AND SUBTITLE
Uncooled Photon Detectors for IR Imaging

5. FUNDING NUMBERS
N00014-99-1-0630

6. AUTHOR(S)
M. Razeghi, H. Mohseni, Y. Wei, A. Gin, J. Bae, S. Slivken, K. Mi, and S. Darvish

7. PERFORMING ORGANIZATION NAME(S) AND ADDRESS(ES)
Northwestern University
Center for Quantum Devices
2220 Campus Drive, Room 4051
Evanston, IL 60208-3129

8. PERFORMING ORGANIZATION
REPORT NUMBER

9. SPONSORING / MONITORING AGENCY NAME(S) AND ADDRESS(ES)
Office of Naval Research
800 N. Quincy Street
Arlington, VA 22217-5660

20030121 111

11. SUPPLEMENTARY NOTES

The views, opinions and/or findings contained in this report are those of the author(s) and should not be construed as an official Office of Naval Research position, policy or decision, unless so designated by other documentation.

12 a. DISTRIBUTION / AVAILABILITY STATEMENT

Approved for public release; distribution unlimited.

12 b. DISTRIBUTION CODE

13. ABSTRACT (Maximum 200 words)

Throughout the comprehensive research in the past three years, the unique properties of Type II InAs/GaSb heterojunctions were utilized for the realization of novel uncooled infrared photodetectors with higher operating temperature, detectivity and uniformity than the commonly available infrared detectors. We have successfully demonstrated uncooled photon detectors in the long wavelength infrared range from 8 μm to 12 μm based on Type II InAs/GaSb superlattices. Photoconductors were grown on GaAs substrates or on GaSb substrates with AlSb insulating layer. Photodiodes were grown on GaAs, GaSb substrates. Wet chemical etching and dry etching techniques have been developed successfully. For photoconductors at room temperature, a detectivity of $1.08 \times 10^8 \text{ cmHz}^{1/2}/\text{W}$ at 11 μm and an effective carrier lifetime of 26 ns have been achieved. For photodiodes at room temperature, we have obtained a detectivity of $1.2 \times 10^8 \text{ cmHz}^{1/2}/\text{W}$ at 7 μm , and $R_0A = 1.36 \times 10^{-2} \Omega\text{cm}^2$, better than HgCdTe ($\sim 10^{-4} \Omega\text{cm}^2$). Detector-laser measurements have shown a response time of less than 68 ns for these detectors. However, some properties are still far from the focal plane array application requirements. The detector performance still needs to be improved in the continuation of the program, especially the detectivity and R_0A .

14. SUBJECT TERMS

15. NUMBER OF PAGES
60

16. PRICE CODE

17. SECURITY CLASSIFICATION
OR REPORT
UNCLASSIFIED

18. SECURITY CLASSIFICATION
ON THIS PAGE
UNCLASSIFIED

19. SECURITY CLASSIFICATION
OF ABSTRACT
UNCLASSIFIED

20. LIMITATION OF ABSTRACT
UL

Abstract:

Throughout the comprehensive research in the past three years, the unique properties of Type II InAs/GaSb heterojunctions were utilized for the realization of novel uncooled infrared photodetectors with higher operating temperature, detectivity and uniformity than the commonly available infrared detectors. We have successfully demonstrated uncooled photon detectors in the long wavelength infrared range from 8 μm to 12 μm based on Type II InAs/GaSb superlattices. Photoconductors were grown on GaAs substrates or on GaSb substrates with AlSb insulating layer. Photodiodes were grown on GaAs, GaSb substrates. Wet chemical etching and dry etching techniques have been developed successfully. For photoconductors at room temperature, a detectivity of $1.08 \times 10^8 \text{ cmHz}^{1/2}/\text{W}$ at 11 μm and an effective carrier lifetime of 26 ns have been achieved. For photodiodes at room temperature, we have obtained a detectivity of $1.2 \times 10^8 \text{ cmHz}^{1/2}/\text{W}$ at 7 μm , and $R_0A = 1.36 \times 10^{-2} \Omega\text{cm}^2$, better than HgCdTe ($\sim 10^{-4} \Omega\text{cm}^2$). Detector-laser measurements have shown a response time of less than 68 ns for these detectors. However, some properties are still far from the focal plane array application requirements. The detector performance still needs to be improved in the continuation of the program, especially the detectivity and R_0A .

I. Introduction

Infrared (IR) detectors are the critical parts of many modern medical, industrial, military, and scientific instruments and systems. Some examples are thermal imaging systems for early detection of breast cancer, non-invasive glucose monitoring, fast engine inspection in the aviation industry, infrared active countermeasure, and laser RADAR. The demand for high performance IR detectors in these systems has driven academic and industrial research and development toward exploration of new material systems as well as device structures. Currently, the most commonly used material in the infrared systems is HgCdTe. Although it is the most studied semiconductor after silicon and germanium, it still cannot provide the required performance due to several physical limitations. Some of these include non-uniformity of the composition due to the high Hg vapor pressure, low mechanical strength and radiation hardness due to the weak atomic bonding, and high tunneling current due to the low electron effective mass.

Type II InAs/GaSb superlattices have been proposed as an alternative to HgCdTe for the strategic windows of 3-5 μm and 8-12 μm as well as longer wavelengths. Unlike HgCdTe, Type II superlattices are constructed from the III-V material system, and hence they have much better mechanical properties and material uniformity. The electron effective mass in these superlattices is higher than the electron effective mass in HgCdTe and InAsSb, therefore the tunneling current is less. The bandgap of the superlattice can be changed to cover a wide IR range (from $\sim 2\mu\text{m}$ to above $25\mu\text{m}$) by changing the thickness of the layers rather than the material composition. Also, in comparison to quantum well infrared photodetectors (QWIPs), Type II superlattices have a much higher quantum efficiency while they do not require surface gratings for absorption of normal incident light.

Despite such inherent advantages, only a few successful IR detectors based on Type II superlattices have been demonstrated recently. The major difficulties in the realization of Type II detectors are the design of the optimum superlattice structure, the growth of high quality material, and the processing.

The goal of our study is to exploit the advantages of Type II superlattices for the realization of high performance infrared detectors at room temperature. First, comprehensive theoretical modeling has been developed for the simulation of the band structure of the Type II superlattices as well as the simulation of the detectors. Using these simulation programs, the optimum superlattice and detector structures for higher

operating temperatures and higher quantum efficiencies have been derived. In parallel, the optimum conditions for the growth of these superlattices have been determined based on their structural, optical, and electrical characterization. Finally, for the fabrication of the devices, several processing techniques such as wet and dry etching of the superlattice structures have been developed.

II. Realization of Uncooled Type II Photoconductors in the Long Wavelength IR range

II.A. Motivation

II.A.1. The Need for Uncooled Photon IR Detectors

Currently available photon detectors have low operating temperatures, and hence require cryogenic coolers. However, in most of the applications, these coolers are not desirable because of their short lifetime and the added power consumption, weight, volume, and costs. Commercially available uncooled IR imaging sensors use ferroelectric or microbolometer detector arrays. These sensors are inherently slow and cannot detect rapid scene changes needed for many applications. Some of the applications which require a fast detector response time ($\tau < 30$ msec) are: free-space communication, proximity fuzes, active infrared countermeasure systems, missile detection/situational awareness for highly maneuvering airborne platforms, LIDARs, gated-imaging, and night vision systems. Thus there is a need for the development of high-speed uncooled detectors in order to meet the requirements of present and future applications.

II.A.2. Problems of Currently Available Photon Detectors

Although photon detectors have gigahertz bandwidths, their high temperature detectivity is severely degraded due to several physical limitations. The existing infrared photon detectors can be categorized as interband, which are mostly HgCdTe and InAsSb, or intersubband quantum well infrared detectors (QWIP). There are some fundamental limitations, namely fast Auger recombination rate in the interband detectors and high thermal generation rate in the intersubband detectors, which drastically decrease their performance and ability for high operating temperature. Moreover, the difficulty of the growth, nonuniformity due to high sensitivity to the composition, and large tunneling currents in HgCdTe and the required sophisticated processing for normal incidence light coupling in n-type QWIPs are the other drawbacks of the currently available IR photon detectors.

II.A.3. Advantages of Type II Superlattices for Uncooled IR Detection

In comparison to HgCdTe, the higher effective mass of electrons and holes and the slower Auger recombination rate^{1,2} lead to lower dark current and higher operating temperature in Type II superlattices. Another advantage of a Type II superlattice is the possibility of bandgap engineering. Unlike bulk material or Type I superlattices, one can modify the energy of the conduction and valence minibands of a Type II superlattice with a high degree of freedom. Recently, II-VI HgTe/CdTe and III-V InAs/Ga_xIn_{1-x}Sb Type II superlattices have shown very promising results in the long wavelength ranges^{3,4}.

II.B. Material System

InAs, GaSb, and AlSb and their related compounds form a nearly lattice matched family of semiconductors known as the 6.1 Å family, since the lattice constants of these material are about $a=6.1$ Å. Figure 1(a) shows their energy gaps and lattice constants compared to the other major semiconductors, while Figure 1(b) shows their energy band lineups.

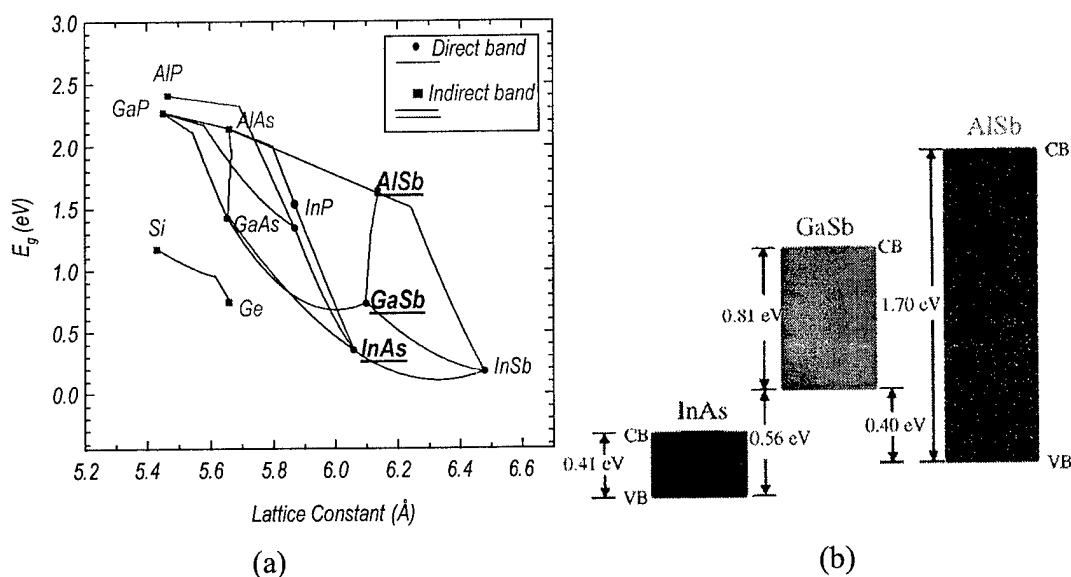


Figure 1 (a) The energy gap and lattice constant of InAs, GaSb, and AlSb and related ternaries compared to the other major semiconductors. (b) The energy band lineups of InAs, GaSb, and AlSb.

The following table shows some of the important properties of the 6.1 Å family:

| Parameters@300K (unless indicated otherwise) | InAs | GaSb | AlSb |
|--|---|--------------------------------------|--|
| Lattice constant (Angstrom) | 6.058 | 6.094 | 6.136 |
| Density (g/cm ³) | 5.70 | 6.61 | 4.26 |
| Melting point (K) | 1215 | 985 | 1338 |
| Expansion coefficient | 4.52×10^{-6} | 6.2×10^{-6} | 4×10^{-6} |
| Thermal conductivity(WK ⁻¹ cm ⁻¹) | 0.48 | 0.4 | ~0.7 |
| Energy gap (electron volt) | 0.356@300K 0.414@77K | 0.7@300K ----@77K | 1.63@300K 1.666@77K |
| Electron mobility(cm ² /v.s) | 20000@300K 35000@77K | 5000@300K -----@77K | 200@300K -----@77K |
| Hole mobility(cm ² /v.s) | 480@300K ----@77K | 880@300K 2400@77K | 375@300K -----@77K |
| Electron effective mass | 0.023m ₀ | 0.042m ₀ | 0.12 |
| Hole effective mass | 0.42 m ₀ | 0.4 m ₀ | 0.98 m ₀ |
| LO phonon energy at zone center | 29.6meV | 28.8meV | 42.1meV |
| TO phonon energy at zone center | 26.9meV | 27.7meV | 39.5meV |
| Refractive index | 3.42@10μm 3.52@3.7μm 4.56@0.517μm | 3.84@10μm 3.79@2μm 3.92@1.55μm | 2.995@20μm 2.08@15μm 3.1@10μm 3.3@2μm |
| Dielectric constant (static) | 15.15 | 15.7 | 12.04 |

Table I. Some of the important properties of InAs, GaSb, and AlSb.

The maximum lattice mismatch in this material system is about $\pm 0.6\%$, and hence many high quality structures can be designed within the critical thickness of the layers. It is also possible to balance the mismatch of the heterostructure or superlattice such that the average lattice constant of the structure is equal to the substrate. Another advantage of this material system is the wide range of energy gaps as well as band lineups that are available. Superlattices based on InAs, GaSb, and AlSb layers can be designed with tunable bandgaps from about 1.6 eV down to zero (semi-metal), while conduction band offsets above 1.4 eV and valence band offsets up to 0.6 eV are possible.

II.C. Modeling and Simulation of the Superlattices Using k·p Method

II.C.1. Energy Band Modeling

The modeling of the superlattice energy bands is a necessary step in the realization of Type II infrared detectors since it provides crucial information about the bandgap of the superlattice and the electron and hole wavefunctions. Based on this information, one can design a superlattice structure for a specific cut-off wavelength with maximized absorption coefficient and carrier lifetime.

The basis for such modeling is the *envelope function approximation* in which the band structure of a periodic or non-periodic heterojunction (superlattices or quantum wells) can be modeled. In this approximation, we assume that the electron or hole wavefunctions consist of two parts: a periodic part due to the regular crystal periodicity, and an envelope part due to the heterojunction. The envelope modulates the periodic part and is assumed to be much larger than it.

Assuming a heterojunction of material A and B, the electron wavefunction, $\psi(\mathbf{r})$, can be written as:

$$\Psi(\mathbf{r}) = \sum_l f_l^{(A,B)}(\mathbf{r}) \cdot u_l(\mathbf{r}) \quad (1)$$

where \mathbf{r} is the position vector in real space, $f_l^{(A,B)}(\mathbf{r})$ is the envelope function in layer A and B, and $u_l(\mathbf{r})$ is the periodic part of the Bloch function, and l runs over as many bands as are included in the analysis. The envelope functions can be decomposed into components that are in-plane and perpendicular to the A-B junction:

$$f_l^{(A,B)}(\mathbf{r}_\perp, z) = \frac{1}{\sqrt{S}} e^{i\mathbf{k}_\perp \cdot \mathbf{r}_\perp} \chi_l^{(A,B)}(z) \quad (2)$$

where \mathbf{r}_\perp and z are the perpendicular and parallel to the growth direction vectors, $\mathbf{k}_\perp = (k_x, k_y)$ is the perpendicular wavevector, S is the area of the sample, and $\chi_l^{(A,B)}(z)$ is the parallel envelope function for band l . The main goal is the calculation of the χ functions. The Hamiltonian for the heterojunction is:

$$H = \frac{p^2}{2m_0} + V_A(\mathbf{r})Y_A + V_B(\mathbf{r})Y_B \quad (3)$$

where p is the momentum, m_0 is electron mass, $V_A(\mathbf{r})$ and $V_B(\mathbf{r})$ are the atomic potential in layers A and B, and $Y_A \equiv 1$ in layer A and zero otherwise, and $Y_B \equiv 1$ in layer B and zero otherwise. We have:

$$H u_{l,0}(\mathbf{r}) = (E_{l,0}^{(A)} Y_A + E_{l,0}^{(B)} Y_B) u_{l,0}(\mathbf{r}) \quad (4)$$

where $u_{l,0}(\mathbf{r})$ is the periodic wavefunction and $E_{l,0}$ is the energy of band l at $\mathbf{k}=0$. Now applying the Hamiltonian to $\psi(\mathbf{r})$ and simplifying it, we find that the χ functions should fulfill the following for energy E :

$$\mathbf{D}\chi = E\chi \quad (5)$$

where $\chi=(\chi_l, \chi_m, \dots)$ is an $1 \times N$ vector of χ_l for N different bands and \mathbf{D} is a $N \times N$ matrix with elements $D_{l,m}$ as following:

$$D_{l,m} = \left[E_{l,0}^{(A)} Y_A + E_{l,0}^{(B)} Y_B + \frac{\hbar^2 \mathbf{k}_\perp^2}{2m_0} - \frac{\hbar^2}{2m_0} \frac{\partial^2}{\partial z^2} \right] \delta_{l,m} + \frac{\hbar \mathbf{k}_\perp}{2m_0} \cdot \langle l | \mathbf{p}_\perp | m \rangle - \frac{i\hbar}{2m_0} \cdot \langle l | p_z | m \rangle \frac{\partial}{\partial z} \quad (6)$$

where $\frac{\partial}{\partial z}$ and $\frac{\partial^2}{\partial z^2}$ are the first and second order derivative operators, l and m are two different bands, and $\delta_{l,m}$ is the dirac-delta function (zero for $l \neq m$ and one for $l=m$). Now it is clear that matrix \mathbf{D} is just the $\mathbf{k} \cdot \mathbf{p}$ matrix of the bulk materials A and B, except that: k_z is replaced with $\frac{\partial}{\partial z}$ and k_z^2 with $\frac{\partial^2}{\partial z^2}$ and $E_{l,0}$ depends on whether one is in layer A or B.

Since the conduction, heavy-hole, light-hole and spin orbit bands have considerable interaction in narrow-gap Type II superlattices, the eight-band $\mathbf{k} \cdot \mathbf{p}$ matrix ($N=8$) was chosen. The 8×8 matrix at $\mathbf{k}_\perp=0$ is decomposed to two 4×4 matrices of \mathbf{D}^\uparrow and \mathbf{D}^\downarrow :

$$\begin{bmatrix} \mathbf{D}^\uparrow & \mathbf{0} \\ \mathbf{0} & \mathbf{D}^\downarrow \end{bmatrix} \begin{bmatrix} \chi^\uparrow \\ \chi^\downarrow \end{bmatrix} = E \begin{bmatrix} \chi^\uparrow \\ \chi^\downarrow \end{bmatrix} \quad (7)$$

Since the spin-up and down are identical at $\mathbf{k}_\perp=0$ ($\mathbf{D}^\uparrow=\mathbf{D}^\downarrow=\mathbf{D}$ and $\chi^\uparrow=\chi^\downarrow=\chi$), eigen-energies are twice degenerate. Matrix \mathbf{D} is:

$$\mathbf{D} = \begin{bmatrix} E_C(z) + \frac{1}{2m_0} p_z F p_z & 0 & -\sqrt{\frac{2}{3}} \Pi p_z & \sqrt{\frac{1}{3}} \Pi p_z \\ 0 & E_{HH}(z) - \frac{1}{2m_0} p_z (\gamma_1 - 2\gamma_2) p_z & 0 & 0 \\ -\sqrt{\frac{2}{3}} \Pi p_z & 0 & E_{LH}(z) - \frac{1}{2m_0} p_z (\gamma_1 + 2\gamma_2) p_z & \frac{\sqrt{2}}{m_0} p_z \gamma_2 p_z \\ \sqrt{\frac{1}{3}} \Pi p_z & 0 & \frac{\sqrt{2}}{m_0} p_z \gamma_2 p_z & E_{SO}(z) - \frac{1}{2m_0} p_z \gamma_1 p_z \end{bmatrix} \quad (8)$$

where Π , γ_1 , γ_2 , and F , are semiconductor parameters and can be found in semiconductor data books such as Landolt-Bornstein. $E_C(z)$, $E_{HH}(z)$, $E_{LH}(z)$, and $E_{SO}(z)$ are the energy of the conduction, heavy-hole, light-hole, and spin-orbit split-off bands at $\mathbf{k}=0$ in the bulk semiconductors. These are functions of position since at different z values different layers of semiconductor with different band energies exist. Although the energy of

different bands at $\mathbf{k}=0$ is readily known for most of the binary and ternary semiconductors, the *band lineup* of two semiconductors at their heterojunction needs to be calculated.

II.C.2. Band Alignment Modeling

The theoretical calculation of the band lineups at semiconductor heterojunctions has been a difficult task, especially since experiments show a wide range of measured values. Although many different models have been suggested⁵ for such calculations, they are not convenient for our modeling, since they require huge computations. Model-solid theory⁶ provides a simple yet accurate method for the calculation of the band lineups. It also does not require *a posteriori* for the strain effect, since strain will directly appear in the deformation potentials.

Assuming that a_s is the lattice constant of the substrate and a_e is the lattice constant of the epi-layer, the strain field parallel to the junction is:

$$\varepsilon_{\parallel} = \frac{a_s}{a_e} - 1 \quad (9)$$

The strain in the perpendicular direction is:

$$\varepsilon_{\perp} = -D\varepsilon_{\parallel} \quad (10)$$

and the value of D for different crystal orientation is:

$$D^{001} = 2\frac{c_{12}}{c_{11}}; \quad D^{110} = \frac{c_{11} + 3c_{12} - 2c_{44}}{c_{11} + c_{12} + 2c_{44}}; \quad D^{111} = 2\frac{c_{11} + 2c_{12} - 2c_{44}}{c_{11} + 2c_{12} + 4c_{44}} \quad (11)$$

where c_{11} , c_{12} , and c_{44} are elastic constants of the epilayer.

When the strain is along [001], the position of the heavy-hole, light-hole, and spin-orbit bands can be calculated from:

$$\begin{aligned} E_{HH} &= E_{V,av} + a_v(2\varepsilon_{\parallel} + \varepsilon_{\perp}) + \frac{\Delta_0}{3} - \frac{1}{2}\delta E_{001} \\ E_{LH} &= E_{V,av} + a_v(2\varepsilon_{\parallel} + \varepsilon_{\perp}) - \frac{\Delta_0}{6} + \frac{1}{4}\delta E_{001} + \frac{1}{2}\left[\Delta_0^2 + \Delta_0\delta E_{001} + \frac{9}{4}(\delta E_{001})^2\right]^{1/2} \\ E_{SO} &= E_{V,av} + a_v(2\varepsilon_{\parallel} + \varepsilon_{\perp}) - \frac{\Delta_0}{6} + \frac{1}{4}\delta E_{001} - \frac{1}{2}\left[\Delta_0^2 + \Delta_0\delta E_{001} + \frac{9}{4}(\delta E_{001})^2\right]^{1/2} \end{aligned} \quad (12)$$

where $E_{V,av}$ is the average valence band energy and Δ_0 is the spin-orbit to valence band gap. a_v is the hydrostatic deformation potential of the valence band and $\delta E_{001} = 2b(\varepsilon_{\perp} - \varepsilon_{\parallel})$ where b is the shear deformation potential.

The conduction band can be calculated from:

$$E_c = E_{V,av} + (a_v + a_c)(2\varepsilon_{||} + \varepsilon_{\perp}) + \frac{\Delta_0}{3} + E_g \quad (13)$$

where a_c is the hydrostatic deformation potential of the conduction band and E_g is the bandgap of the semiconductor.

II.C.3. Energy Band Numerical Simulation

a. Periodic Structures

The Envelope Function Approximation was used to numerically simulate the band structure of the superlattices. The system of differential equations that governs the wavefunctions can be constructed from the relative values of the band edge energies E_c , E_{LH} , E_{HH} , E_{SO} , and the equation $\mathbf{D}\chi = E\chi$ from the previous sections. This system can be solved with a proper set of boundary conditions. A periodic structure implies a periodic wavefunction or: $\chi(z+L) = \chi(z)$, where L is the period of the structure (a superlattice or multi quantum well). It can be shown that the energy E , which satisfies the boundary conditions, for a two-layer periodic structure is the solution of:

$$\cos(k_z(a+b)) = \cos(k_1 a) \cos(k_2 b) - \frac{1}{2} \cdot \left(\frac{k_1 \mu_2}{k_2 \mu_1} + \frac{k_2 \mu_1}{k_1 \mu_2} \right) \cdot \sin(k_1 a) \sin(k_2 b) \quad (14)$$

where a and b are the thickness of layer 1 and 2 in the superlattice and k_z is the superlattice momentum in the z (growth) direction. The constants k_i and μ_i are defined for $i=1,2$ (layer 1 and 2) as:

$$\begin{cases} k = \sqrt{\frac{3 \cdot (E_c - E)((E_{LH} - E)(E_{SO} - E) - 0.5 \cdot \delta E_{001}^2)}{\hbar^2 \Pi^2 (2 \cdot (E_{SO} + \delta E_{001} - E) + E_{LH} - E)}} \\ \mu = \frac{3 \cdot (0.5 \cdot \delta E_{001}^2 - (E_{LH} - E)(E_{SO} - E))}{\Pi^2 (2 \cdot (E_{SO} - \delta E_{001} - E) + E_{LH} - E)} \end{cases} \quad (15)$$

where E_c , E_{LH} , E_{SO} , and δE_{001} are calculated as described in the previous section. Π is the Kane parameter which is explained in the "Energy Band Modeling" section. For the heavy-hole band:

$$\begin{cases} k = \frac{1}{\hbar} \cdot \sqrt{2m_{HH}(E_{HH} - E)} \\ \mu_i = -m_{HH} \end{cases} \quad (16)$$

where E_{HH} is the heavy-hole energy at $\mathbf{k}=0$, and m_{HH} is the heavy-hole effective mass.

Figure 2 shows the solution of equation (59) calculated by a program written in Mathcad⁷. The results of the calculated optical transition energies based on this model shows excellent agreement with our recent experimental results on p-i-n Type II photodiodes⁸.

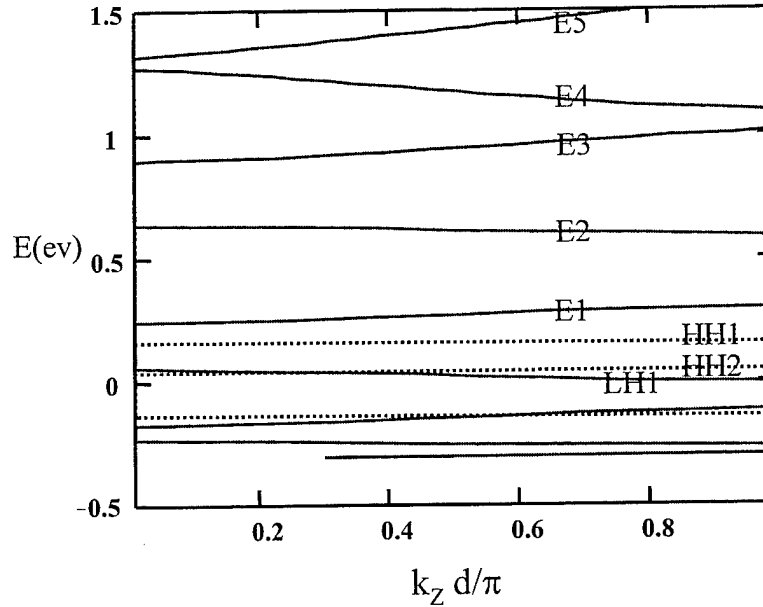


Figure 2. The calculated energy band dispersion of a InAs/GaSb (48Å/48Å) superlattice. k_z is the momentum in the growth direction, and $d=a+b$ is the period of the superlattice.

b. Aperiodic Structures

In the case of an aperiodic structure, the above simulation technique cannot be used since the periodic boundary condition is no longer valid. However, the differential equation derived from $\mathbf{D}\chi = E\chi$ can still be solved numerically. The Runge Kutta Fehlberg method was chosen as the numerical technique to solve the system of differential equations, since it is proven to provide high accuracy and speed. Another advantage of this technique is that if one uses the 5th order, the error of the computation can be predicted. This feature is used in the program to adjust the step size of the independent variable (in this case position z) of the differential equation to keep the error below a given value.

The program, written in C++, is capable of calculating the allowed energy states of the heterostructures as well as the electron and hole wavefunctions associated to each

energy state. Figure 3 shows an example of the simulated electron wavefunctions and energies of two states at the edge of a Type II superlattice detector. The magnitude of the electron wavefunctions shows that the quantum wells next to the GaSb buffer layer have a lower chance of occupation compared to the rest of the wells in the superlattice.

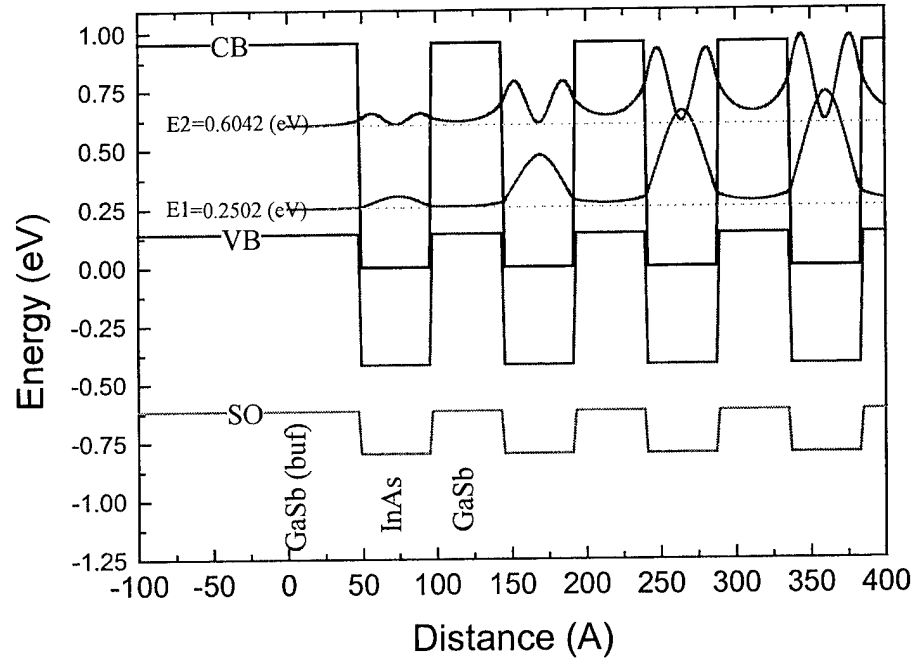


Figure 3. Two calculated electron energy states and their wavefunctions in the active region of a Type II superlattice detector. CB, VB, and SO are the conduction, valence, and spin-orbit bands of different layers.

II.D. Modeling and Simulation of the Superlattices Using Empirical Tight-Binding Method (ETBM)

ETBM originated from the work of J. C. Slater and G. F. Koster in 1954.⁹ The method was originally called Linear Combinations of Atomic Orbitals (LCAO). The atomic orbitals are indeed Wannier functions¹⁰ (for theoretical study) or Lowdin orbitals¹¹ (for practical calculations). Wannier functions and Lowdin orbitals are orthogonal at different atomic sites, while actual atomic orbitals are not. The ETBM use parameter fitting to simplify numerical calculations, and is different from the *ab initio* tight binding method¹² which involves calculations of many difficult two center integrals that are in general not practical. We treat those integrals as parameters to fit the experimental band structure information and pseudopotential results at certain symmetry points in the 1st Brillouine zone for bulk III-V materials, and then plug these fitted parameters into superlattice Hamiltonian. We have reduced the number of independent energy interaction terms using the symmetry of the crystal. ETBM can be used to treat III-V semiconductors without magnetic structures.

The ETBM is capable of calculating the bandstructure in the entire Brillouine zone, and simulating arbitrary Bravais lattice structures with basis at atomic level. This gives us the freedom to do calculations with very thin layers in superlattices, including the interfaces which are only one monolayer thick.

There are different levels of modeling in ETBM. For bulk materials, according to their accuracy, there are sp^3s^* nearest neighbor model¹³, sp^3s^* second nearest neighbor with spin-orbit interactions model¹⁴, $sp^3d^5s^*$ nearest neighbor with spin-orbit interactions model¹⁵, etc. For superlattices, there are sp^3s^* second nearest neighbor without spin-orbit interactions model^{16,17}, sp^3 second nearest neighbor with spin-orbit interactions model¹⁸, etc. Among all these levels, we have chosen sp^3s^* nearest neighbor modeling with spin-orbit interactions. This level of modeling have the accuracy we need and with fairly less amount of calculations we can handle.

Another issue we have taken into account is the stress and strain effects. The stress and strain are naturally embedded into the Hamiltonian using the well-known d^2 scaling rule. The deformation potential calculations used in $k \cdot p$ modeling are not needed. The effects of the stress or strain on the bandstructure can be calculated directly.

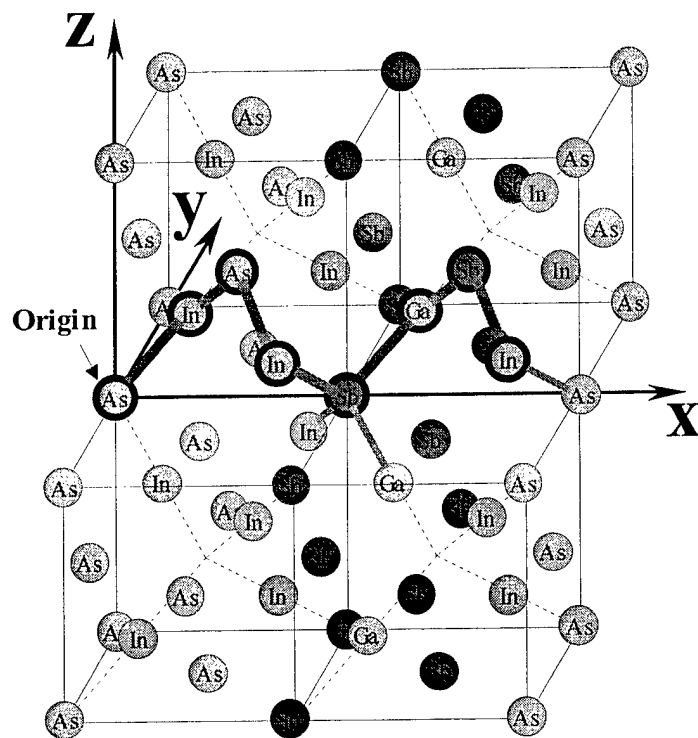
Before we write down the Bloch wavefunction for the electrons, we need to identify the simplest unit cell for the system to reduce all redundant calculations and shorten the calculation time. For bulk III-V materials, the unit cell we choose consists of two

adjacent group III and group V atoms. For superlattice materials, the choosing of unit cells is illustrated in Figure 4.

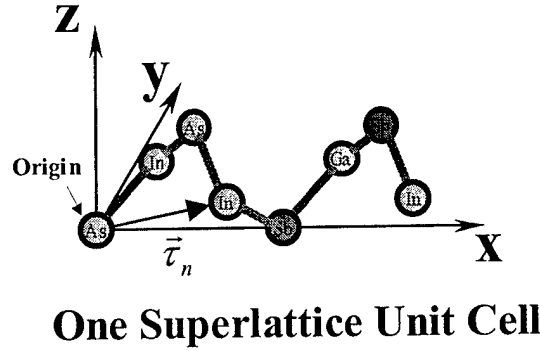
Assuming the construction Lowdin orbitals for the bulk or superlattices is:

$$\varphi_n^\alpha(\vec{r} - \vec{R} - \vec{\tau}_n) \quad (17)$$

where n runs through all the atoms in a unit cell, τ_n are the coordinate position vectors of the atoms in the cell, α runs through all considered types of Lowdin orbitals (s, p, s*, etc.), and R represent the coordinate position vector of the unit cell in the entire material we are considering.



(a)



(b)

Figure 4 (a) One superlattice example of $[(\text{InAs})_2\text{-InSb-(GaSb)}_1]_n$; (b) The simplest unit cell chosen for ETBM calculations.

Now we can construct the Bloch wavefunction of electrons for the entire material:

$$\Psi_{\vec{k}}(\vec{r}) = \sum_{\vec{R}_{SL}} \sum_{\alpha} \sum_{n=1}^N \exp(i\vec{k} \cdot (\vec{R} + \vec{\tau}_n)) A_n^{\alpha} \varphi_n^{\alpha}(\vec{r} - \vec{R} - \vec{\tau}_n) \quad (18)$$

where N is the total number of atoms in one unit cell, A_n^{α} are constants, and \vec{R}_{SL} runs through all the unit cells.

The bandstructure calculation problem now reduced to an eigenvalue problem for $\Psi_{\vec{k}}(\vec{r})$:

$$H\Psi_{\vec{k}}(\vec{r}) = E\Psi_{\vec{k}}(\vec{r}) \quad (19)$$

where H is the Hamiltonian for the material under investigation, and E is the energy eigenvalues that are dependent on \vec{k} values in the 1st Brillouin zone. Using the orthogonal properties of the Lowdin orbitals, we can rewrite the eigenvalue problem in the following format:

$$\sum_{\vec{R}_{SL}} \sum_{\alpha} \sum_{n=1}^N \exp(i\vec{k} \cdot (\vec{R} + \vec{\tau}_n - \vec{R}' - \vec{\tau}_m)) \cdot A_n^{\alpha} \iiint_{\infty} d\vec{r}^3 \varphi_m^{\beta *}(\vec{r} - \vec{R}' - \vec{\tau}_m) H \varphi_n^{\alpha}(\vec{r} - \vec{R} - \vec{\tau}_n) = E \cdot A_m^{\beta} \quad (20)$$

For nearest neighbor approximation, \vec{R}_{SL} runs through only those nearest cells. For the tetrahedral structures, the summation over \vec{R}_{SL} will be reduced to closed forms and a practical set of equations for numerical calculations can be obtained. The only difference between bulk material and superlattice is the number of atoms in one calculation unit cell. Therefore the matrix size for superlattices is proportional to the real space period in the growth direction. Figure 5 shows a general format of the Hamiltonian matrix for the bulk material. Figure 6 shows a representative band diagram in the entire 1st Brillouin zone along typical symmetry directions for bulk InSb. The short blue horizontal lines in the diagram are the energy levels at certain symmetry points from the Landolt Bornstein New Series for semiconductor materials. Figure 7 shows one calculated band diagram for the superlattice of $[(\text{InAs})_{20}\text{-InSb-(GaSb)}_{13}]_n$ along growth direction and the in plane direction.

| | | | | | | | | | |
|--|--|---|---|--|--|---|--|--|--|
| $E_{sa,sa}^0$ | 0 | 0 | 0 | 0 | $\frac{(g_1^* + f_1) \cdot 4E_{sa,sc}^0}{4E_{sa,sc}^0}$ | $\frac{(g_2^* + f_2) \cdot 4E_{sa,xc}^0}{4E_{sa,xc}^0}$ | $\frac{(-g_2^* + f_2) \cdot 4E_{sa,xc}^0}{4E_{sa,xc}^0}$ | $\frac{(-g_1^* + f_1) \cdot 4E_{sa,xc}^0}{4E_{sa,xc}^0}$ | 0 |
| 0 | $E_{pa,pa}^0$ | $-\frac{i}{3}\Delta_a$ | $\frac{1}{3}\Delta_a$ | 0 | $\frac{(-g_2^* - f_2) \cdot 4E_{xa,sc}^0}{4E_{xa,sc}^0}$ | $\frac{(g_1^* + f_1) \cdot 4E_{xa,xc}^0}{4E_{xa,xc}^0}$ | $\frac{(-g_1^* + f_1) \cdot 4E_{xa,yc}^0}{4E_{xa,yc}^0}$ | $\frac{(-g_2^* + f_2) \cdot 4E_{xa,yc}^0}{4E_{xa,yc}^0}$ | $\frac{(-g_2^* - f_2) \cdot 4E_{xa,s^*c}^0}{4E_{xa,s^*c}^0}$ |
| 0 | $\frac{i}{3}\Delta_a$ | $E_{pa,pa}^0$ | $-\frac{i}{3}\Delta_a$ | 0 | $\frac{(g_2^* - f_2) \cdot 4E_{xa,sc}^0}{4E_{xa,sc}^0}$ | $\frac{(-g_1^* + f_1) \cdot 4E_{xa,yc}^0}{4E_{xa,yc}^0}$ | $\frac{(g_1^* + f_1) \cdot 4E_{xa,xc}^0}{4E_{xa,xc}^0}$ | $\frac{(g_2^* + f_2) \cdot 4E_{xa,yc}^0}{4E_{xa,yc}^0}$ | $\frac{(g_2^* - f_2) \cdot 4E_{xa,s^*c}^0}{4E_{xa,s^*c}^0}$ |
| 0 | $\frac{1}{3}\Delta_a$ | $\frac{i}{3}\Delta_a$ | $E_{pa,pa}^0$ | 0 | $\frac{(g_1^* - f_1) \cdot 4E_{xa,sc}^0}{4E_{xa,sc}^0}$ | $\frac{(-g_2^* + f_2) \cdot 4E_{xa,yc}^0}{4E_{xa,yc}^0}$ | $\frac{(g_2^* + f_2) \cdot 4E_{xa,xc}^0}{4E_{xa,xc}^0}$ | $\frac{(g_1^* + f_1) \cdot 4E_{xa,xc}^0}{4E_{xa,xc}^0}$ | $\frac{(g_1^* - f_1) \cdot 4E_{xa,s^*c}^0}{4E_{xa,s^*c}^0}$ |
| 0 | 0 | 0 | 0 | E_{s^*a,s^*a}^0 | 0 | $\frac{(g_2^* + f_2) \cdot 4E_{s^*a,xc}^0}{4E_{s^*a,xc}^0}$ | $\frac{(-g_2^* + f_2) \cdot 4E_{s^*a,xc}^0}{4E_{s^*a,xc}^0}$ | $\frac{(-g_1^* + f_1) \cdot 4E_{s^*a,xc}^0}{4E_{s^*a,xc}^0}$ | 0 |
| $\frac{(g_1 + f_1^*) \cdot 4E_{sa,sc}^0}{4E_{sa,sc}^0}$ | $\frac{(-g_2 - f_2^*) \cdot 4E_{xa,sc}^0}{4E_{xa,sc}^0}$ | $\frac{(g_2 - f_2^*) \cdot 4E_{xa,sc}^0}{4E_{xa,sc}^0}$ | $\frac{(g_1 - f_1^*) \cdot 4E_{xa,sc}^0}{4E_{xa,sc}^0}$ | 0 | $E_{sc,sc}^0$ | 0 | 0 | 0 | 0 |
| $\frac{(g_2 + f_2^*) \cdot 4E_{sa,xc}^0}{4E_{sa,xc}^0}$ | $\frac{(g_1 + f_1^*) \cdot 4E_{xa,xc}^0}{4E_{xa,xc}^0}$ | $\frac{(-g_1 + f_1^*) \cdot 4E_{xa,yc}^0}{4E_{xa,yc}^0}$ | $\frac{(-g_2 + f_2^*) \cdot 4E_{xa,yc}^0}{4E_{xa,yc}^0}$ | $\frac{(g_2 + f_2^*) \cdot 4E_{s^*a,xc}^0}{4E_{s^*a,xc}^0}$ | 0 | $E_{pc,pc}^0$ | $-\frac{i}{3}\Delta_c$ | $\frac{1}{3}\Delta_c$ | 0 |
| $\frac{(-g_2 + f_2^*) \cdot 4E_{sa,xc}^0}{4E_{sa,xc}^0}$ | $\frac{(-g_1 + f_1^*) \cdot 4E_{xa,yc}^0}{4E_{xa,yc}^0}$ | $\frac{(g_1 + f_1^*) \cdot 4E_{xa,xc}^0}{4E_{xa,xc}^0}$ | $\frac{(g_2 + f_2^*) \cdot 4E_{xa,yc}^0}{4E_{xa,yc}^0}$ | $\frac{(-g_2 + f_2^*) \cdot 4E_{s^*a,xc}^0}{4E_{s^*a,xc}^0}$ | 0 | $\frac{1}{3}\Delta_c$ | $E_{pc,pc}^0$ | $-\frac{i}{3}\Delta_c$ | 0 |
| $\frac{(-g_1 + f_1^*) \cdot 4E_{sa,xc}^0}{4E_{sa,xc}^0}$ | $\frac{(-g_2 + f_2^*) \cdot 4E_{xa,yc}^0}{4E_{xa,yc}^0}$ | $\frac{(g_2 + f_2^*) \cdot 4E_{xa,yc}^0}{4E_{xa,yc}^0}$ | $\frac{(g_1 + f_1^*) \cdot 4E_{xa,xc}^0}{4E_{xa,xc}^0}$ | $\frac{(-g_1 + f_1^*) \cdot 4E_{s^*a,xc}^0}{4E_{s^*a,xc}^0}$ | 0 | $\frac{1}{3}\Delta_c$ | $\frac{i}{3}\Delta_c$ | $E_{pc,pc}^0$ | 0 |
| 0 | $\frac{(-g_2 - f_2^*) \cdot 4E_{xa,s^*c}^0}{4E_{xa,s^*c}^0}$ | $\frac{(g_2 - f_2^*) \cdot 4E_{xa,s^*c}^0}{4E_{xa,s^*c}^0}$ | $\frac{(g_1 - f_1^*) \cdot 4E_{xa,s^*c}^0}{4E_{xa,s^*c}^0}$ | 0 | 0 | 0 | 0 | 0 | $E_{sc,sc}^0$ |

Figure 5 Representation of the Hamiltonian matrix for bulk III-V tetrahedral structures. The energy terms remains as fitting parameters and f, g are geometric factors related with the tetrahedral structure. Δ_a , Δ_c are the spin-orbit interaction terms for anions and cations.

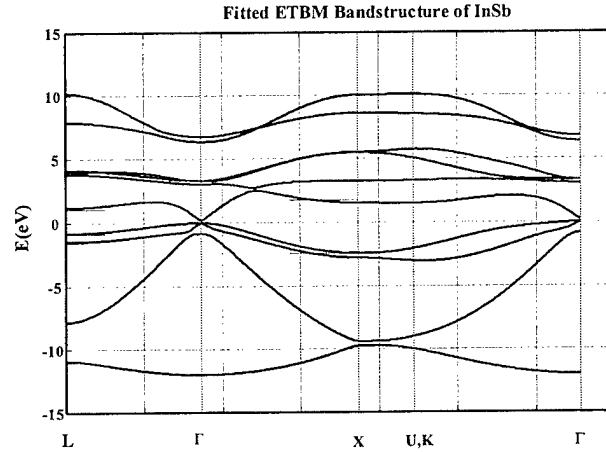


Figure 6 Representative bandstructure for InSb at liquid nitrogen temperature for the entire 1st Brillouin zone along typical symmetry directions. The short horizontal blue lines in the band diagram are energy levels from Landolt-Bornstein New Series for semiconductor materials.

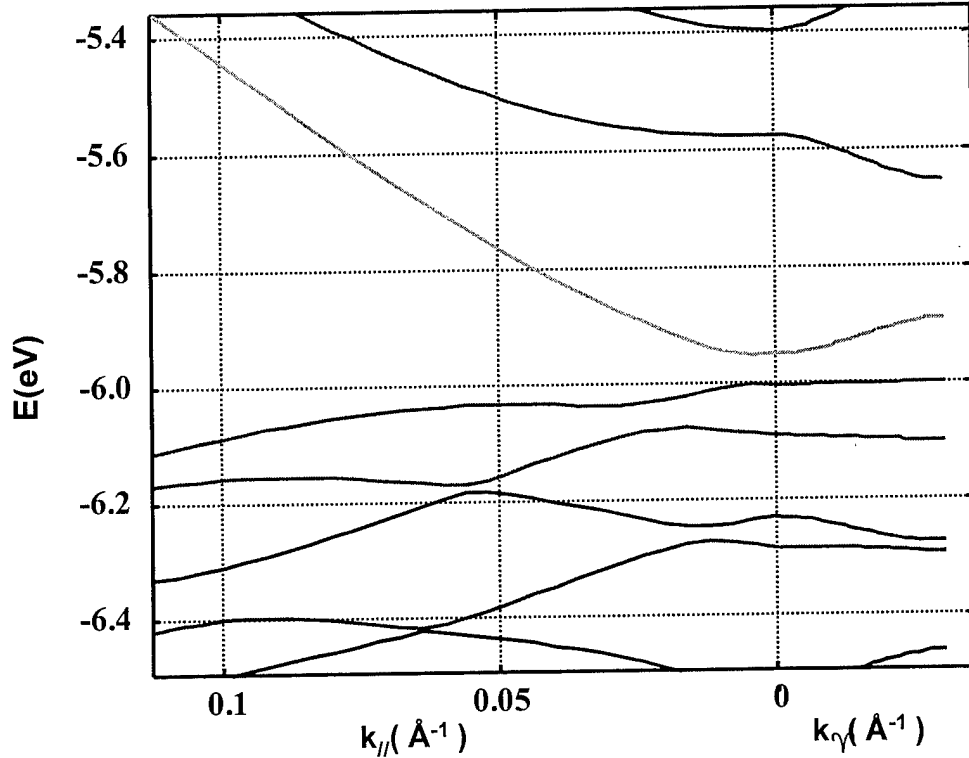


Figure 7 Calculated band structure for superlattice: $[(\text{InAs})_{20}\text{-InSb-(GaSb)}_{13}]_n$ along the growth direction and the inplane direction.

II.E. Modeling and Simulation of the Devices

In the previous chapters the modeling and simulation methods required for optimizing the superlattice structure was described. However, modeling and simulations at the device level are also necessary tools for the optimization of detectors. The key issue is maximizing the detectivity of the device. It can be shown that the detectivity is independent of the device area. Therefore, the only parameter is the thickness of the active layer. The thicker the active layer, the higher the internal quantum efficiency is since the optical absorption will be higher. However, a thicker active layer means a lower resistivity, and hence higher noise. The detectivity of the device can be calculated from the responsivity and the noise as indicated by equation (22)

The responsivity of the device as function of the SL thickness, t is:

$$R_i(t) = \frac{q\lambda\tau(\mu_e + \mu_h)V_B(1-r)}{hcl^2}(1 - e^{-\alpha t}) \quad (21)$$

where t is the thickness of the superlattice, q is the electron charge, λ is the infrared wavelength, τ is the carrier lifetime, μ_e and μ_h are electron and hole in-plane mobilities, V_B is the voltage bias, r is the reflectivity of the sample, h is the Planck constant, c is the speed of light, l is the device length, and α is the absorption coefficient at λ .

The current noise of the device is also a function of the device conductance which depends on the buffer layer and device thickness. Here we consider the major noise components that are Johnson and generation-recombination noises. Johnson noise of the device is:

$$i_{n,\text{Johnson}}(t) = \sqrt{4kT \{q(n\mu_e + p\mu_h)t + \sigma_B t_B\} \frac{A_d}{l^2} \Delta f} \quad (22)$$

where k is the Boltzmann constant, T is the temperature, n and p are the electron and hole concentrations, σ_B is the buffer layer conductance, and t_B is the GaSb buffer layer thickness. The generation-recombination noise can be calculated from:

$$i_{n,\text{GR}}(t) = \left\{ \frac{2qV_B(\mu_e + \mu_h)}{l^2} \right\} \cdot \sqrt{\left(\frac{np}{n+p} \cdot \frac{\tau}{1 + \omega^2 \tau^2} \right) A_d t \Delta f} \quad (23)$$

where ω is the angular frequency and $\omega^2 \tau^2 \ll 1$ in this experiment. The total current noise of the device can be calculated from:

$$i_n = \sqrt{i_{n,\text{Johnson}}^2 + i_{n,\text{GR}}^2} \quad (24)$$

A program in Mathcad was written which calculates the responsivity and detectivity of the device versus the superlattice thickness. The input data for the program are the mobility and concentration of electrons and holes (extracted from Hall measurement), the absorption coefficient (extracted from FTIR measurement), and carrier lifetime (extracted from noise and responsivity measurements). Figure 8 shows the calculated¹⁹ detectivity of a device versus superlattice thickness for three different GaSb buffer layer thickness.

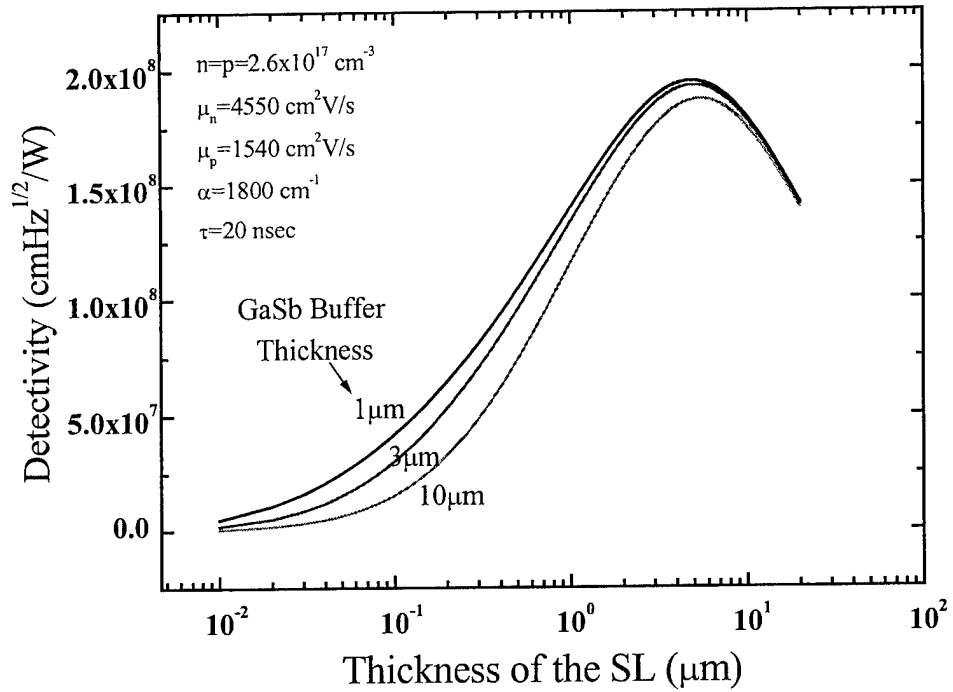


Figure 8. The calculated detectivity of a device versus the thickness of the superlattice with different GaSb buffer layer thickness. n and p are electron and hole concentrations, μ_n and μ_p are their mobilities. α is the optical absorption coefficient and τ is the carrier lifetime.

II.F. Growth

After the design of the superlattice layer thickness for the target wavelength and the simulation of the device for optimum superlattice thickness, the superlattices were grown by molecular beam epitaxy (MBE) on semi-insulating GaAs substrates. The reactor is an Intevac Modular Gen II MBE machine with uncracked As and Sb, and elemental Ga, In, and Al source material. A 4 μm GaSb buffer layer was grown directly on 3" GaAs substrates. The wafer was then broken into $\sim 1 \text{ cm}^2$ pieces and indium-mounted to molybdenum blocks. InAs is found to have a very narrow window for planar growth, while high quality GaSb can be grown in a wider range of growth conditions when reflection high energy electron diffraction (RHEED) showed a 1×3 reconstruction pattern (see Figure 9). The optimum growth conditions for InAs layers were found to be: $T=400^\circ\text{C}$ according to a pyrometer, a V to III incorporation rate ratio ≈ 3 , and a growth

rate of 0.5 monolayer/s. In this condition, RHEED showed 2×4 reconstruction patterns. The pyrometer is calibrated with the temperature of the transition from a 1×5 to a 1×3 reconstruction pattern in the GaSb buffer layers. Based on the theoretical modeling and simulation we chose the optimum structure for a room temperature detector at $\lambda = 11 \mu\text{m}$. The structure consisted of a $t = 2 \mu\text{m}$ superlattice with 48 \AA InAs, 30 \AA GaSb, one monolayer of InSb at the interfaces as it is shown to improve the optical and electrical quality of the superlattice²⁰. Finally, the superlattice was capped with a thin 200 \AA GaSb layer.

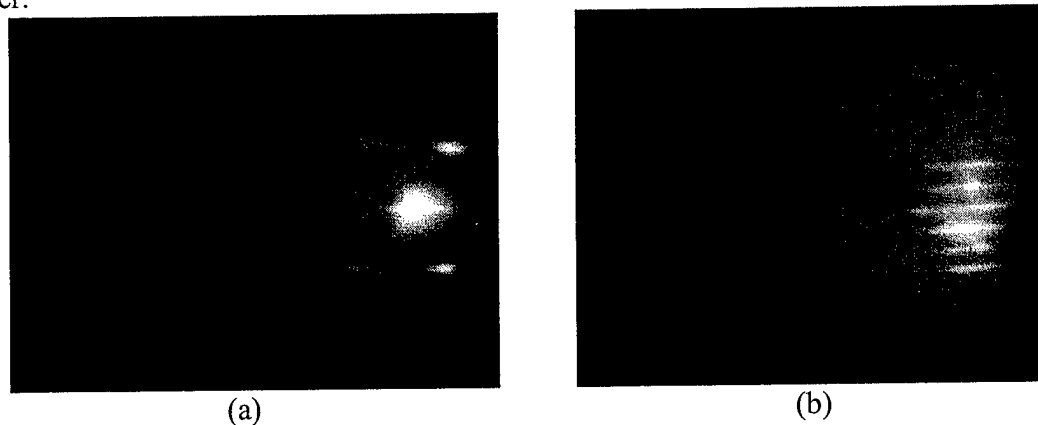


Figure 9. The RHEED of the GaSb surface shows the $1 \times$ pattern (a), and the $3 \times$ pattern (b) these patterns are 90° apart in the azimuthal direction.

II.G. Characterization

The quality of the superlattices was assessed by structural, electrical, and optical characterization.

II.G.1. Structural Characterization

High resolution x-ray diffraction was used to investigate the structure of the material. X-ray diffraction simulation has also been performed to verify the superlattice structures. Figure 10 shows the typical x-ray diffraction of the Type II superlattices and the simulation results. Sharp x-ray peaks up to the 5th order satellite were observed. This is an indication of high crystal quality and superlattice uniformity in the samples, despite more than 6% mismatch between the lattice constant of the superlattices and the GaAs substrates²¹. This figure also shows the reproducibility of the growth, since the second sample was grown a week after the first one.

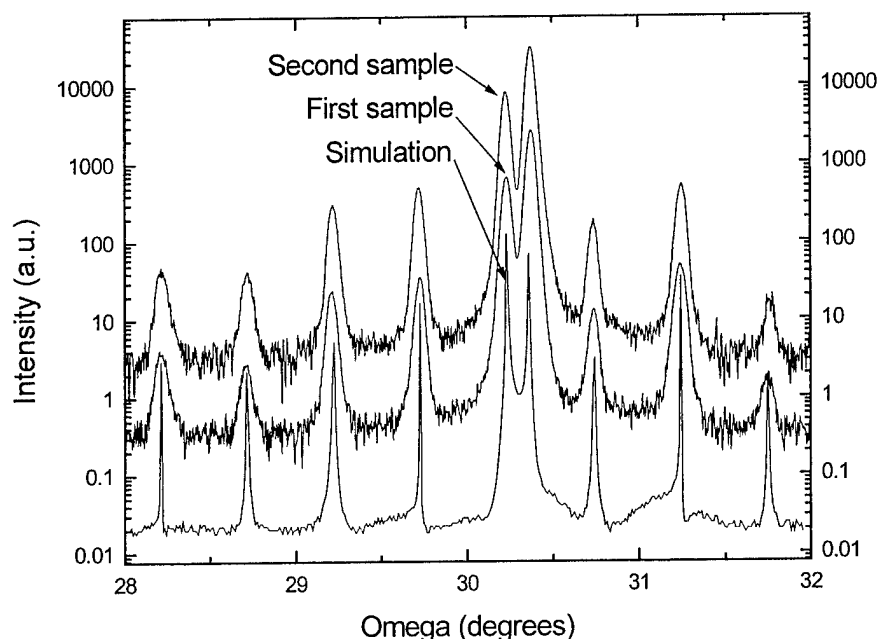


Figure 10. High resolution x-ray diffraction of two samples and the simulation result. Although one of the samples was grown one week after the other, they are almost identical and the simulation is also in good agreement with them.

Figure 10 shows that the mismatch between the average lattice constant of the SL and the lattice constant of the GaSb buffer layer is about 0.3%. The full width at half maximum (FWHM) of the peaks is about 180 arcsec. Although high quality SLs with thickness of about 0.5 μm can be grown with such mismatch, one has to reduce the mismatch for thicker superlattices. The average lattice constant of the superlattice can be adjusted by changing the thickness of the InAs layer, however this will also change the bandgap of the SL! Interface modification provides a better method to change the average lattice constant of the superlattices with a little effect on their bandgap. As was mentioned before, the interfaces can be either InSb-type or GaAs-type. Although these layers are very thin (about 1 monolayer), they have a considerable effect on the average lattice constant of the SL, since the mismatch between InSb and GaSb is about +0.6% and the mismatch between GaAs and GaSb is -0.6%. Considering the thickness of the interfaces, a precise adjustment of these layers is obviously a difficult task. We managed to routinely grow SLs with very low mismatch to the GaSb buffer layers (see Figure 11) by utilizing two techniques. The atomic beam fluxes Ga, In, Sb, and As were calibrated

with dynamic RHEED technique to below 1% error before each growth. Also, a low growth rate of about 0.5 monolayer per second was used, and therefore the deposition time of the interface was about two seconds which is considerably longer than the actuation time of the shutters in our MBE system (~0.1 second).

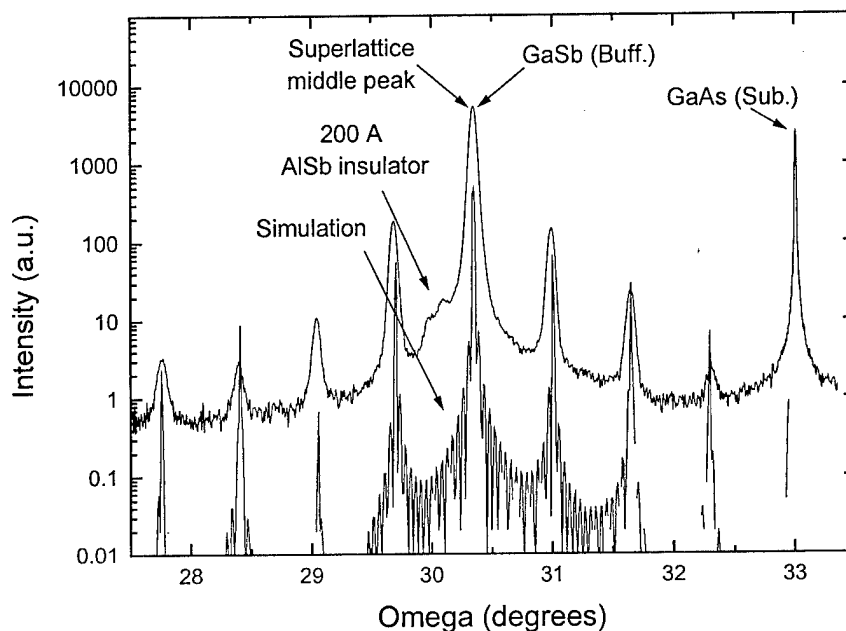


Figure 11. High resolution x-ray diffraction of a superlattice grown on a 200 Å AlSb layer on a GaSb buffer layer. The SL has a lattice mismatch of less than 0.05% to the GaSb buffer layer.

The surface morphology of the samples was also assessed with a Digital Instruments Nanoscope IIIa atomic force microscope. The root mean square (rms) roughness of the surface is less than 5 Å (see Figure 12) which is comparable to the rms roughness of the samples grown on lattice matched GaSb substrates.

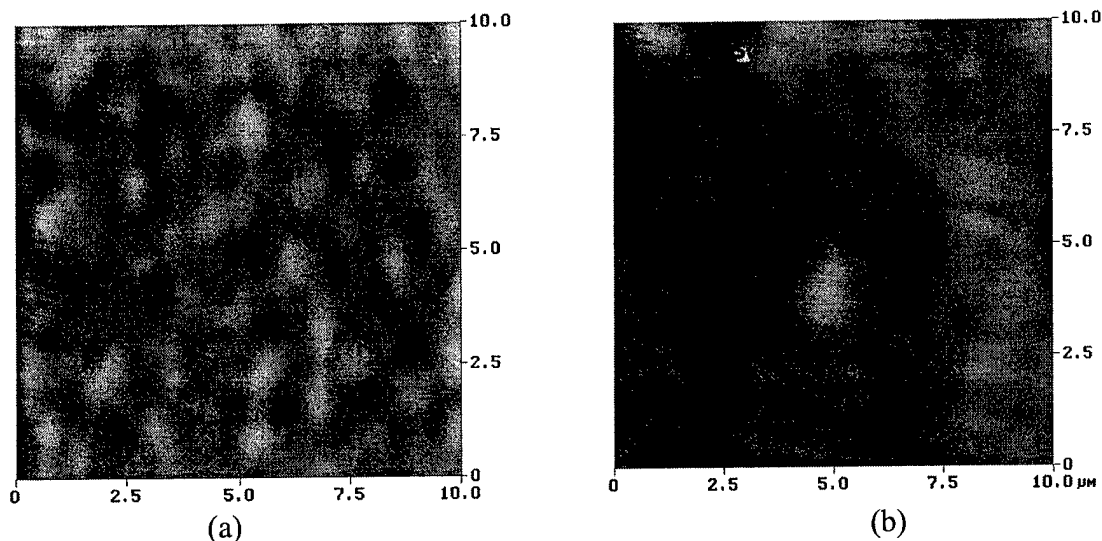


Figure 12. (a) AFM image of the surface of a GaSb buffer on GaAs substrate shows a root mean square (rms) roughness of about 4.2 Å. (b) The surface morphology of the sample after the growth of the superlattice on top of the buffer layer. The rms roughness is about 4.9 Å.

II.G.2. Optical Characterization

A Mattson Instrument Galaxy 3000 Fourier transform infrared (FTIR) spectrometer was used to obtain the optical characteristics of the superlattices. Figure 13 shows the room temperature optical absorption spectra of the superlattice²². The effect of the substrate and GaSb buffer layer was removed by measuring the background with a substrate and GaSb buffer layer. The oscillatory features between 0.3 eV to 0.5 eV are due to the interference of internal reflections inside the SL (Fabry Perot oscillation). Since the light path length during the background measurement was not identical to the sample measurement, we could not eliminate the atmospheric absorption effects. The features around 0.175 eV (~ 6-7 μm) are artifacts due to the high atmospheric absorption in this wavelength from water vapor absorption lines.

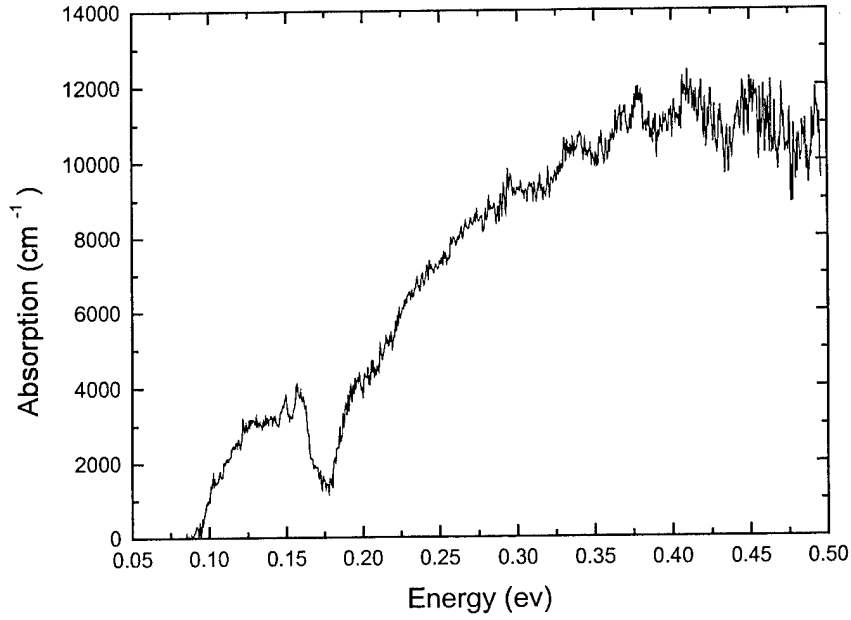


Figure 13. Room temperature absorption spectra of a 0.5 μm thick sample. The absorption at 0.12 eV is comparable to the absorption of HgCdTe with similar bandgap.

II.G.3. Electrical Characterization

Since electrons and holes are confined in InAs and GaSb respectively, we could not use the Hall measurement technique on superlattices because of the high sheet density of electrons and holes in the InAs and GaSb layers. The overall Hall coefficient for this material R_H , and conductance ρ , with two dominant channels of electrons and holes can be approximated as:

$$R_H = \frac{\sigma_{xy}/B}{\sigma_{xy}^2 + \sigma_{xx}^2}; \quad \rho = \frac{\sigma_{xx}}{\sigma_{xy}^2 + \sigma_{xx}^2} \quad (25)$$

where:

$$\sigma_{xx} = q \left(\frac{n\mu_e}{1 + \mu_e^2 B^2} + \frac{p\mu_h}{1 + \mu_h^2 B^2} \right); \quad \sigma_{xy} = qB \left(\frac{p\mu_h^2}{1 + \mu_h^2 B^2} - \frac{n\mu_e^2}{1 + \mu_e^2 B^2} \right) \quad (26)$$

B is the magnetic field density in the Hall measurement, and μ_e and μ_h are the electron and hole mobilities and n and p are their concentrations. The formula shows clearly that the overall Hall mobility can be much smaller than the real mobility of electrons or holes if σ_{xy} approaches zero. As the transport of electrons is more important for photodetector operation due to its higher mobility, single quantum wells of InAs were grown to examine this property. This provided a simple and fast method for electrical assessment of the interfacial quality. After the optimization of growth conditions, the in-plane room temperature mobility of electrons in a 75 Å InAs well increased from 5,000 to 14,000 $\text{cm}^2/\text{V}\cdot\text{s}$ which is about the half the value of bulk InAs.

For superlattices, field-dependent Hall measurement was used (in collaboration with Wright Laboratory, Wright Patterson Air Force Base) to extract the mobility and concentration of electrons and holes at different temperatures.

Hall coefficient R_H , and lateral conductance ρ , were measured at eight different magnetic flux densities for a Type II superlattice with InAs/GaSb (48Å/48Å). A minimum root mean square method was used for fitting with n, p, μ_e , μ_h , as the fitting parameters to the measured data. Fitting is an accurate method, since there are only four unknowns for sixteen equations. Figure 14 shows the results of this fitting at T=300K. The mobility and concentration of the electrons were calculated as: $\mu_n \sim 4550 \text{ cm}^2/\text{V}\cdot\text{s}$ and $n \sim 1.29 \times 10^{17} \text{ cm}^{-3}$ and for holes: $\mu_p \sim 1540 \text{ cm}^2/\text{V}\cdot\text{s}$ and $p \sim 1.2 \times 10^{17} \text{ cm}^{-3}$ at this temperature.

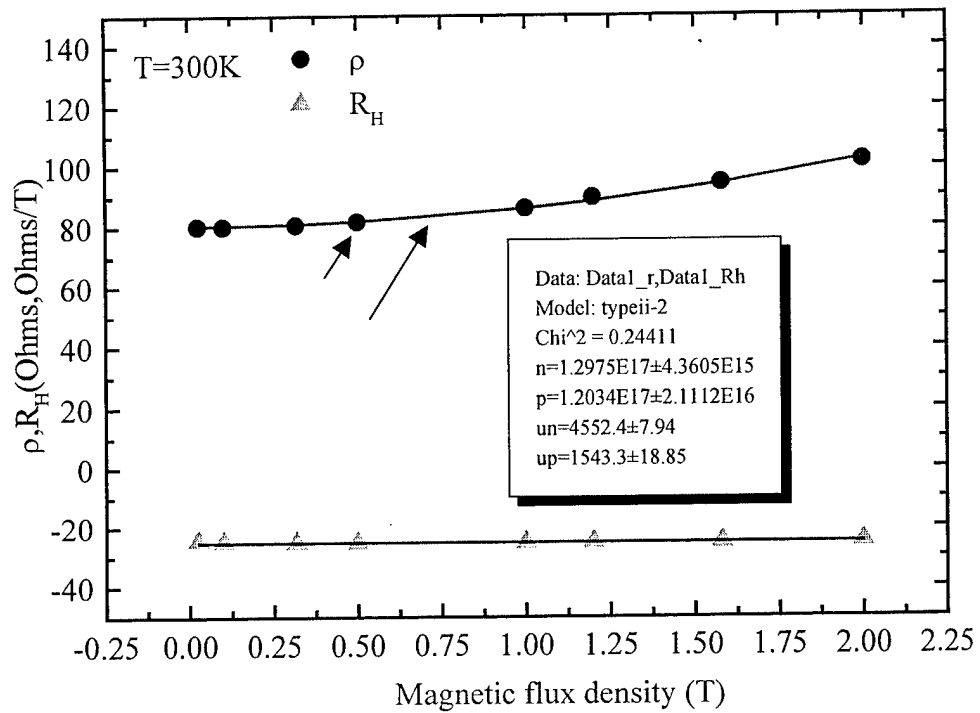


Figure 14. The measured Hall coefficient R_H , and conductance ρ of the superlattice versus B , and the calculated values based on the parameters in the inset box.

Figure 15 shows the results of similar calculation at $T = 120$ K. The fitted curve clearly deviates from the measured ρ at $B \sim 1.25$ T. This is due to the fact that our model only considers electrons and holes with unique mobilities, while in reality each carrier can have several channels with different mobilities.

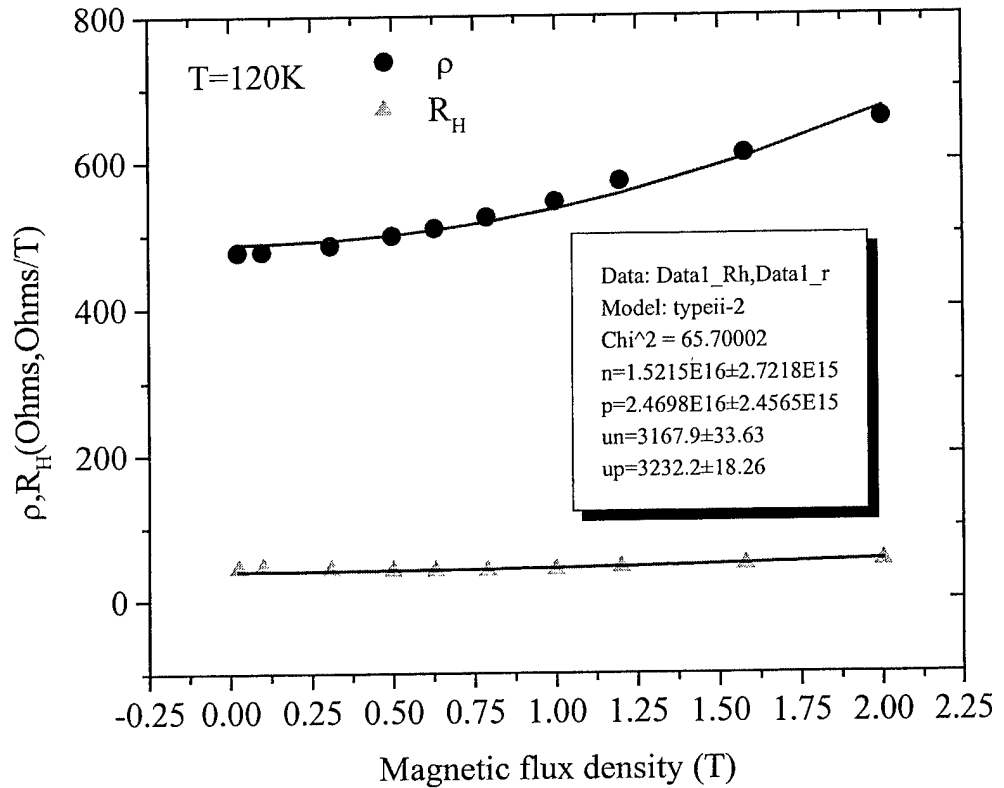


Figure 15. The measured Hall coefficient R_H , and conductance ρ of the superlattice versus B at $T=120$ K. The fitted curve deviates slightly from the measured values of ρ at $B \sim 1.25$ T.

Figure 16 shows the mobility "spectrum" of the carriers in the superlattice, calculated with a program developed at Wright Laboratory. It shows the concentration of the different carriers versus their mobilities. Besides the peak at $\mu=0$ which is due to an artifact, three other peaks are visible that correspond to an electron-type carrier with mobility of about ~ 5000 $\text{cm}^2/\text{v.s}$ and concentration of about $\sim 5 \times 10^{15} \text{ cm}^{-3}$, and two hole-type carriers with mobilities of ~ 3200 and ~ 15000 , and concentrations of $2 \times 10^{16} \text{ cm}^{-3}$, and $4 \times 10^{14} \text{ cm}^{-3}$ respectively.

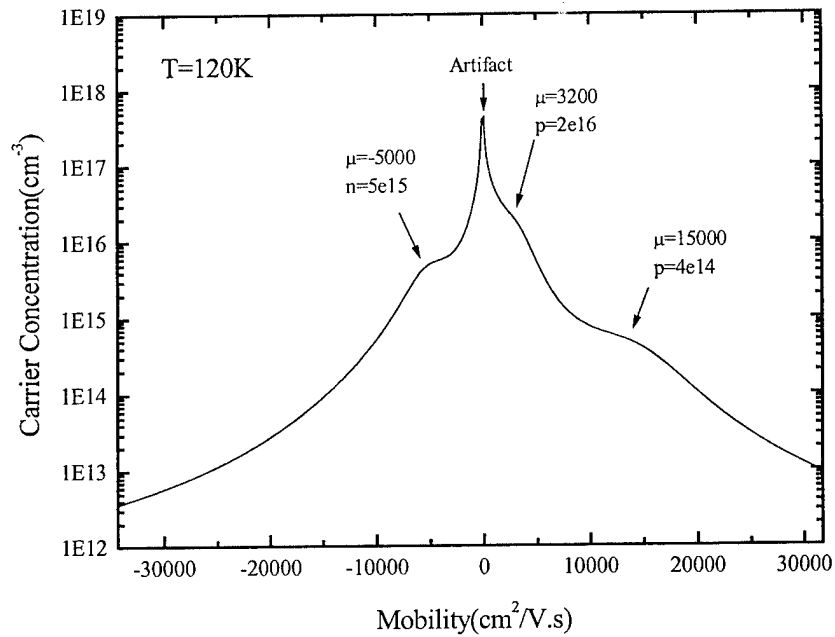


Figure 16. The calculated carrier concentration versus mobility based on the field-dependent Hall measurement method at $T=120\text{K}$.

II.H. Device Processing

II.H.1. Cleaning

The first step in the processing is the cleaning of the sample surfaces from mineral-based and organic-based contaminants. This is an essential step of the processing, since such contamination can act as a mask during chemical etching and also prevent maximum adhesion of the metal contacts. We noticed that a commonly used degreasing solution, Trichloroethylene, attacks the surface of samples that are terminated with GaSb. Therefore, the following cleaning recipe was used:

- 1- Rinse in acetone for 1 min.
- 2- Rinse in boiling methanol for 1 min.
- 3- Rinse under DI water for 3min.
- 4- Repeat steps 1-3
- 5- Blow-dry the samples with dry nitrogen.

II.H.2. Photolithography

The first step of the lithography process is the photoresist (PR) spinning, in which a thin layer of PR is formed on the surface. The thickness of the PR is determined from the PR viscosity and the rotation speed and time. We used an AZ5214PR and rotation speed of 4000 rpm to have a PR thickness of about 1.5 μ m. The next step is a short baking, known as soft baking, of the samples at about 96°C for 50 seconds. The PR coated sample is then exposed with UV light through a chrome-patterned glass mask for a few seconds. There are two types of PR processes: a positive process that makes a duplicate of the original mask and a negative process that makes a negative pattern of the mask. For the positive process, the samples are dipped into a developer solution and the exposed areas will be etched away. For a negative process (liftoff), the samples are baked at about 116°C for 50 seconds, exposed to UV for about 1 minute (without any mask), and then dipped into the developer. The last step for a positive process is a post baking at about 116°C for 50 seconds which improve the adhesion of the PR. An important difference between the positive and negative process is the shape of the PR at the edge of the exposed area. A negative process makes an mushroom shape that is necessary for a successful liftoff process which is mainly used for the definition of the Ohmic contacts (see Figure 17Figure 17.)

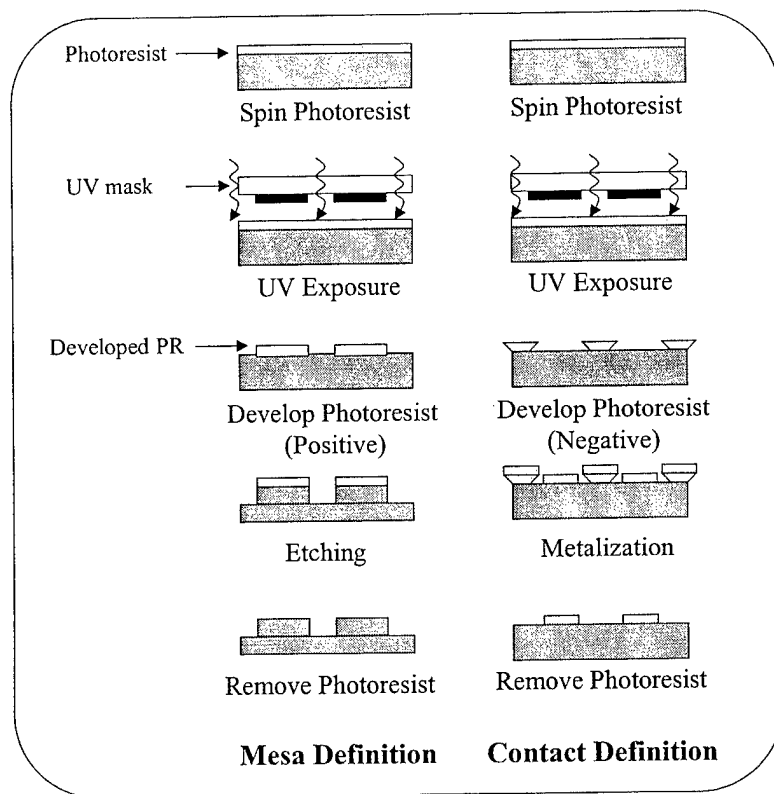


Figure 17. The major processing steps for the definition of the mesa (positive process) and metal contacts (negative process).

II.H.3. Etching

The grown material was etched into mesas with wet (chemical) and dry etching. Several chemical solutions that are commonly used for etching of both GaSb and InAs were studied for uniform and controllable etching of the InAs/GaSb superlattices. These included Br_2 :Methanol, $\text{HF}:\text{HNO}_3:\text{CH}_3\text{-COOH}$, and $\text{CH}_3\text{-COOH}:\text{HCl}:\text{HNO}_3:\text{Br}_2$. However, $\text{H}_3\text{PO}_4:\text{H}_2\text{O}_2:\text{H}_2\text{O}$ (1:1:10), which is used for the etching of InAs, showed the best etching properties. This solution also provides a convenient etching rate of about $0.6\mu\text{m}/\text{min}$. For InAs/GaInSb superlattices a better etching solution is based on $\text{C}_6\text{H}_8\text{O}_7$ (Citric acid) and H_2O_2 . Citric acid is first dissolved in water with a 1gram/ml ratio, the solution is then mixed with an equal volume of H_2O_2 and stored for a few minutes before etching. While the etching rate of about $300\text{\AA}/\text{s}$ is relatively slow, this solution provides a very controllable etching.

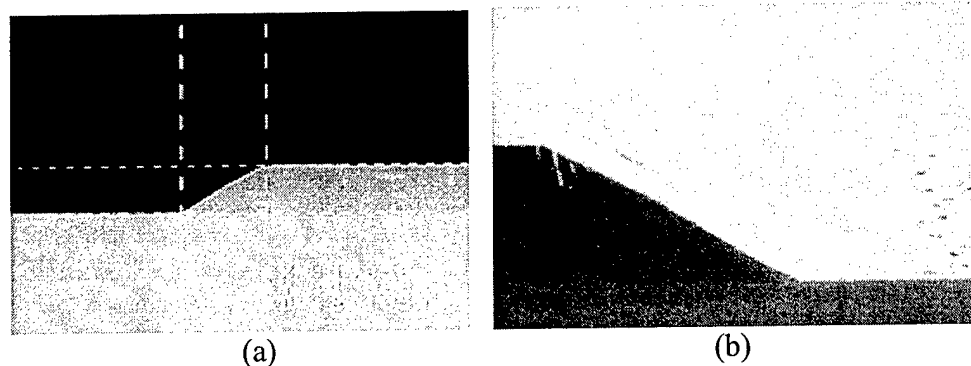


Figure 18. (a) SEM cross section image of a superlattice etched with $C_6H_8O_7$: H_2O : H_2O_2 , and (b) High resolution SEM image of the edge of the mesa shows a clean and smooth etching.

Dry etching techniques were also developed for a higher uniformity over large areas, and more vertical sidewalls. Several different methane and chlorine based recipes were studied. A mixture of BCl_3 :Ar (10 sccm:40 sccm) at a pressure of about 1mTorr, RF power of 100Watt, and microwave power of about 800 Watt showed the best performance. It provided vertical sidewalls as well as (see Figure 19) smooth surfaces under the etched areas. Figure 20 (a) and (b) compares the AFM image and surface roughness of a superlattice before and after dry etching. The roughness is essentially the same over a $20\mu m \times 20\mu m$ area.

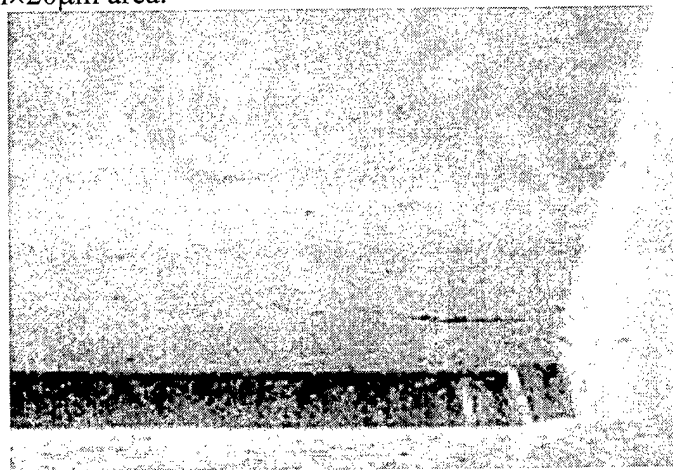


Figure 19. SEM image of the sidewalls of a mesa after $\sim 1\mu m$ dry etching.

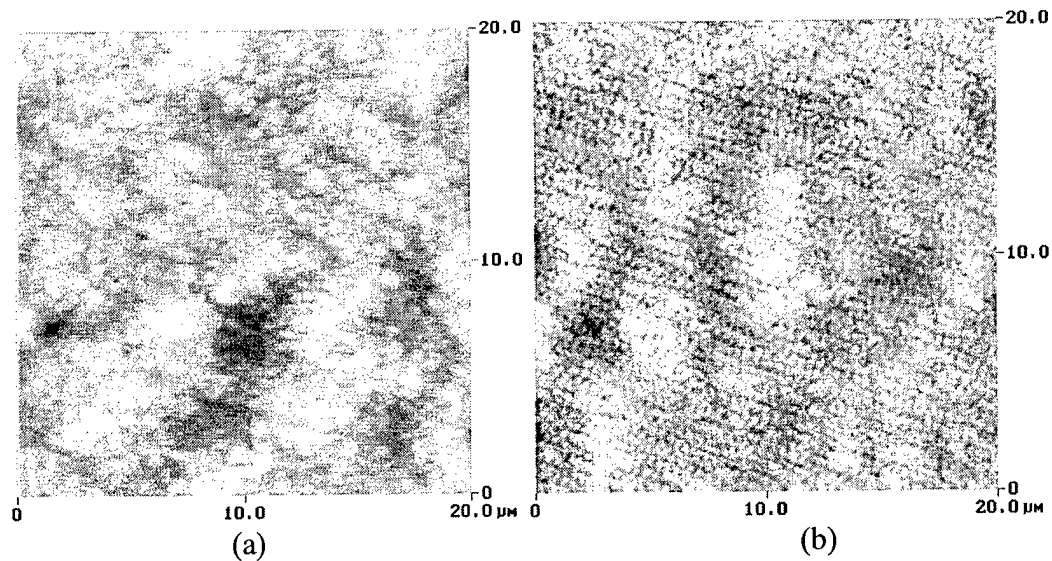


Figure 20. AFM image of the surface of a superlattice (a) before etching rms surface roughness is 7.8 \AA , and (b) after $\sim 1 \text{ }\mu\text{m}$ dry etching the rms surface roughness is 9.5 \AA .

After dry etching the photoresist was removed with a special chemical, AZ 400T photoresist stripper, provided by the photoresist supplier. Although SEM and optical microscope shows a clean surface after this process, AFM image of the surface (see Figure 21-a) shows that there are still a considerable photoresist residuals. This tiny layer can reduce the performance of the device, since it prevents a good adhesion between the metal contact and the superlattice in the metallization step. An oxygen ashing process was used to remove the residual photoresist. It uses an oxygen flow rate of 20 sccm and pressure of 50 mTorr with a RF power of 100 Watts for 40 seconds. Figure 21-b shows the AFM image of the surface after the ashing process. The surface roughness is comparable to the roughness of the superlattice before any process (see Figure 20-a).

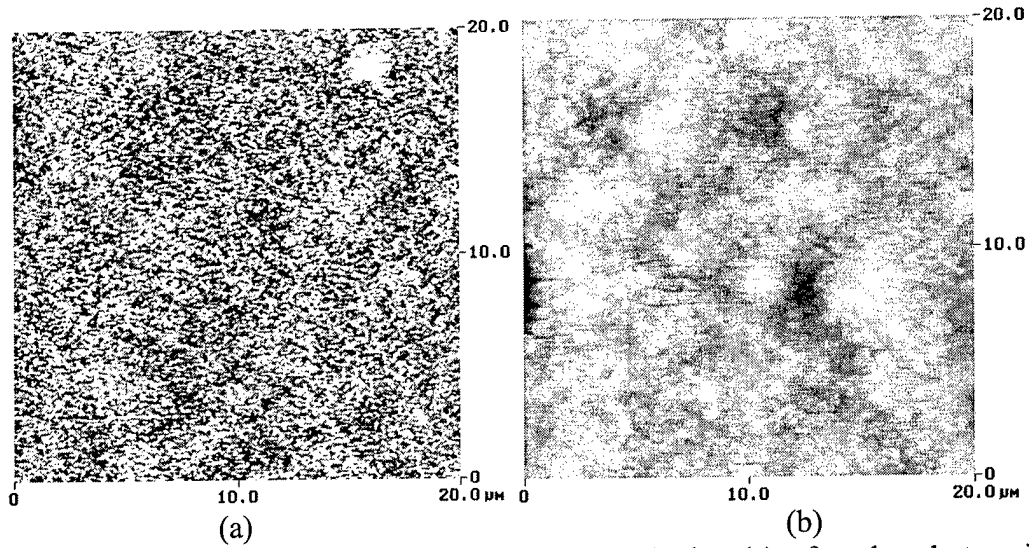


Figure 21. AFM image of the surface of the superlattice (a) after the photoresist is removed with stripper the rms surface roughness is 31.5 \AA , and (b) rms surface roughness is 7.9 \AA after the oxygen ashing process.

II.H.4. Metallization

A standard liftoff technique was used for the definition of the top metal contacts as described in the lithography section. Ti/Au ($400\text{\AA}/1200\text{\AA}$) were evaporated with an electron beam evaporator for the contacts. Figure 22 shows the schematic diagram and the SEM image of the processed device.

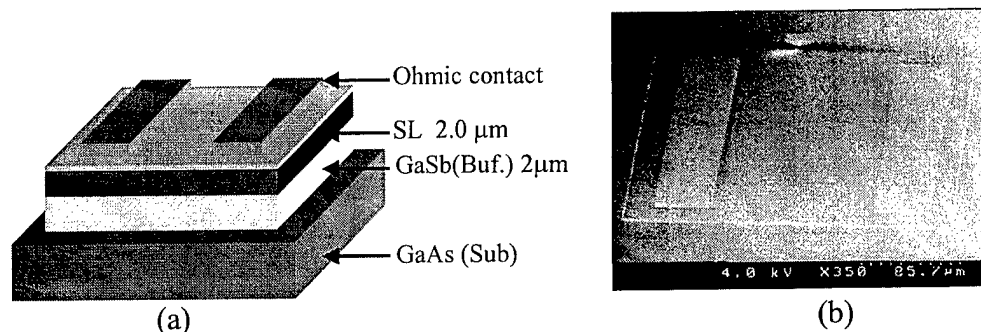


Figure 22. (a) Schematic diagram, and (b) SEM image of the processed device.

II.I. Device Measurements

The samples were then glued to a copper heatsink with an epoxy and attached to the cold finger of a liquid nitrogen cryostat equipped with a temperature controller.

II.I.1. Responsivity

Spectral photoresponse of the device was measured using a Galaxy 3000 FTIR spectrometer system. The samples were illuminated through the front side with normal incidence. The absolute response of the photodetectors was calculated using a blackbody test set, which is composed of a blackbody source (Mikron 305), preamplifier (EG&G PA-6), lock-in amplifier (EG&G 5209), and chopper system (Stanford Research System SR540). Figure 23 shows the responsivity of the device in the 2-17μm wavelength range at 78K and 300K with an in-plane electrical field of 5V/cm.

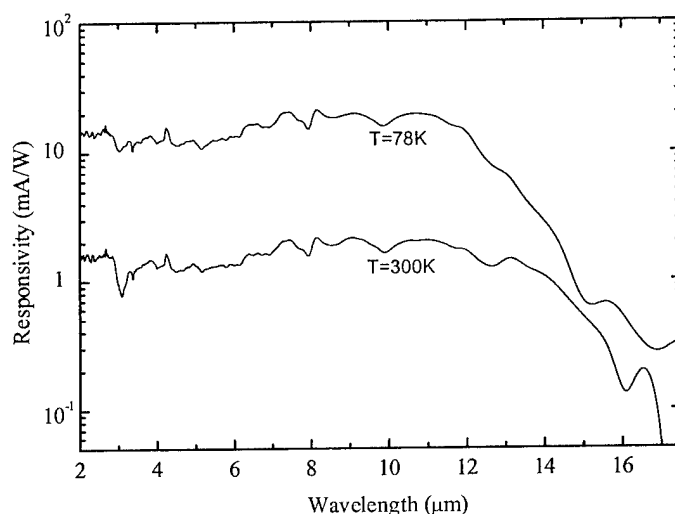


Figure 23. The responsivity spectra of the device at 78K and 300K with an in-plane electrical field of 5V/cm.

To assess the temperature dependence, the current responsivity of the device was measured at $\lambda=10.6\mu\text{m}$ wavelength from 78K to room temperature at a constant electrical field. Figure 24 shows the responsivity of the detector at $\lambda=10.6\mu\text{m}$ versus the detector temperature. In order to see whether current responsivity follows a power function, we fit the data to an allometric function. An allometric fit has a general form of $y=Ax^B$ where x is the variable and A and B are the fitting parameters. This fit shows that the responsivity of the detector is nearly proportional to $T^{-1.93}$.

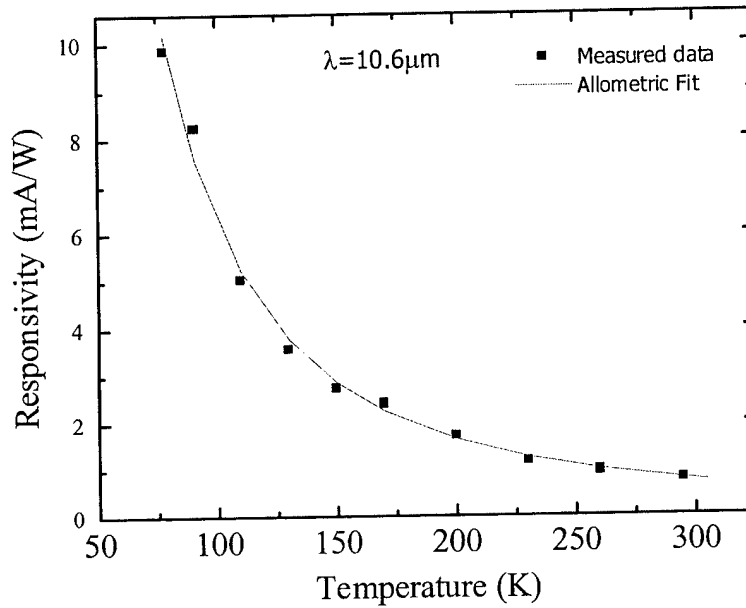


Figure 24. The current responsivity of the device versus temperature at $\lambda=10.6\mu\text{m}$ at constant voltage bias. The squares are the measured points and the line is an Allometric fit (AT^B) to the points which shows that responsivity is nearly proportional to T^{-2} .

This is an unusual behavior since responsivity of the narrow gap material is usually an exponential function of temperature at higher temperatures where Auger recombination is the dominant recombination mechanism. Theoretically, Zegrya et al²³ showed that the Auger recombination rate is a power function of the temperature (proportional to T^2) in Type II heterostructures compared to the exponential function in the bulk semiconductors. Since the current responsivity is proportional to the carrier lifetime (which is dictated by Auger recombination rate, this power dependency of the responsivity indicates a good agreement with the theoretical predictions.

The effective lifetime of the carriers was also extracted from the responsivity and Hall measurements on a $t=0.5\mu\text{m}$ thick superlattice:

$$\tau_{\text{ef}} = \frac{lg}{E(\mu_e + \mu_p)} \quad (27)$$

where $l=2\text{mm}$ is the device length, g is the photoconductor gain, and $E=5\text{V/cm}$ is the electrical field. The gain of the device can be calculated from:

$$g = \frac{R_i hc}{\lambda \eta q} \quad (28)$$

where $R_i=2\text{mA/W}$ is the current responsivity, h is the Planck constant, c is the speed of light, $\lambda=10.6\mu\text{m}$ is the wavelength of the light, η is the quantum efficiency, and q is the electron charge. Assuming an internal quantum efficiency near unity and negligible reflection from the bottom of the superlattice and unpolished backside of the substrate, the quantum efficiency can be calculated from:

$$\eta = (1 - r)(1 - e^{-\alpha t}) \quad (29)$$

where r is the top surface reflection coefficient, $\alpha=1.8 \times 10^3 \text{cm}^{-1}$ is the absorption coefficient of the superlattice and $t=0.5\mu\text{m}$ is the thickness of the superlattice. Assuming $r \approx 0.3$, the quantum efficiency, photoconductive gain, and carrier lifetime can be calculated from above formulas as: $\eta=6.02\%$, $g=3.9 \times 10^{-3}$, and $\tau_{\text{eff}}=26.8\text{nsec}$. The effective lifetime is about an order of magnitude longer than the carrier lifetime in HgCdTe photoconductors with similar bandgap and carrier concentration at room temperature²⁴. Since Auger recombination is the dominant recombination mechanism at room temperature, we believe that the enhancement of carrier lifetime is due to the suppression of Auger recombination in the Type II superlattice.

II.1.2. Noise Measurements

The noise was measured with a fast fourier transform (FFT) spectrum analyzer (Stanford Research System SR 760) and a low noise, wide band pre-amplifier with 54dB voltage gain (EG&G PA-100). Figure 25 shows the input noise spectrum of the FFT analyzer, the output noise spectrum of the shorted pre-amplifier, and the output noise of the pre-amplifier, when it was connected to the detector. The detector was biased by the pre-amplifier at $V_b=5$ volts.

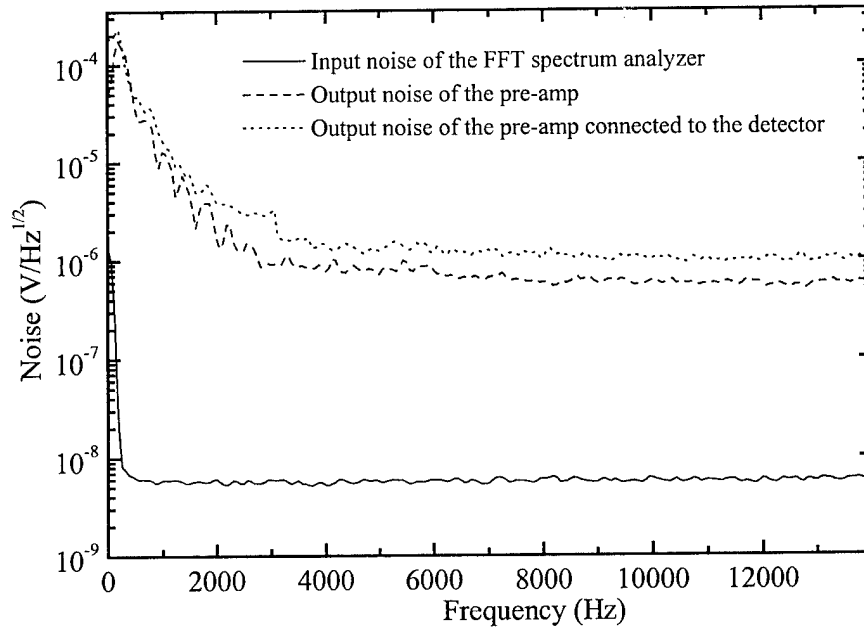


Figure 25. The measured input noise spectrum of the fast Fourier transform (FFT) spectrum analyzer, the output noise spectra of the pre-amplifier with a shorted input and the output noise spectra of the pre-amplifier when it is connected to the detector at 300K.

The mean-square noise of the detector can be modeled as:

$$V_n^2 = V_J^2 + V_{\frac{1}{f}}^2 + V_{GR}^2, \quad (30)$$

where V_n is the overall noise of the detector, V_J is the Johnson-Nyquist noise, $V_{1/f}$ is the $1/f$ noise and V_{GR} is the generation-recombination noise. The value of the Johnson noise can be calculated as

$$V_J^2 = 4kTR\Delta f, \quad (31)$$

where k is the Boltzmann constant, T is the temperature and $R=76$ ohms is the resistance of the device. The value of Johnson noise for the device at room temperature is $1.12\text{nV/Hz}^{1/2}$. The $1/f$ noise can be approximated with:

$$V_{1/f}^2 = V_{GR}^2 \frac{f_{1/f}}{f}, \quad (32)$$

where $f_{1/f}$ is a constant which depends on the sample, and f is the frequency. This shows that at high enough frequencies, $1/f$ noise can be negligible compared to the other two

types of noise. Then the value of the generation-recombination noise can be extracted from the total noise of the device in this range and the value of the Johnson noise. The noise equivalent circuit model²⁵ was used to extract the noise of the photodetector as $V_n=1.7 \text{ nV/Hz}^{1/2}$ above 10kHz. From the above equations, the value of the generation-recombination noise can be calculated as $V_{GR}=1.28 \text{ nV/Hz}^{1/2}$. The generation-recombination noise can be approximated as:

$$V_{GR} = \frac{2V_b}{(lwt)^{1/2}} \cdot \frac{1+b}{bn+p} \cdot \left(\frac{np}{n+p} \cdot \frac{\tau \Delta f}{1+\omega^2 \tau^2} \right)^{1/2} \quad (33)$$

where $w=4\text{mm}$ is the detector width, ω is the angular frequency and $\omega\tau \ll 1$ in this experiment, and b is the ratio of μ_e to μ_p . From the V_{GR} equation, the value of the carrier lifetime can be calculated as $\tau=17\text{nsec}$ which is close to the value of the lifetime extracted from the optical response measurement. It should be noted that the calculation of the carrier lifetime from the electrical noise of the device is not an accurate technique and may only provide a rough estimation for the carrier lifetime.

II.1.3. Response Time Measurement

As was explained in section V.A., one of the motivations for the realization of uncooled photon detectors is the need for uncooled detectors with response times $\tau < 30 \text{ msec}$. Therefore, it was very important to measure the response time of the Type II uncooled detectors. However, conventional methods such as using mechanical choppers could not achieve time accuracy below the millisecond range. We used a room temperature quantum cascade laser, developed at CQD²⁶, as a narrowband and high speed infrared source in our measurement. The schematic diagram of the setup is shown in Figure 26. The pulse generator and laser driver were inside an Avtech AVR-4A-PW which is capable of generating high power electrical pulses with fall time of about 5 nsec.

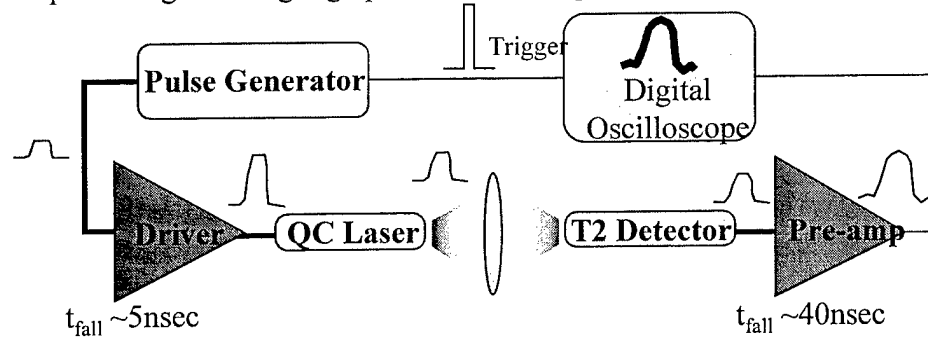


Figure 26. The schematic diagram of the time response measurement setup.

The quantum cascade laser was uncooled and operated at $\lambda=8.5\mu\text{m}$ with a negligible time delay. An EG&G PA-100 low-noise pre-amp was used to amplify the detector signal. Unfortunately, the pre-amp is not very fast and has a fall time of more than 40 nsec. The output signal of the pre-amp was measured with a Tektronix TDS 520B digital oscilloscope. It shows a 90% to 10% fall time of about 68 nsec, as shown in Figure 27, for the whole setup and hence the detector has a fall time below 40nsec²⁸.

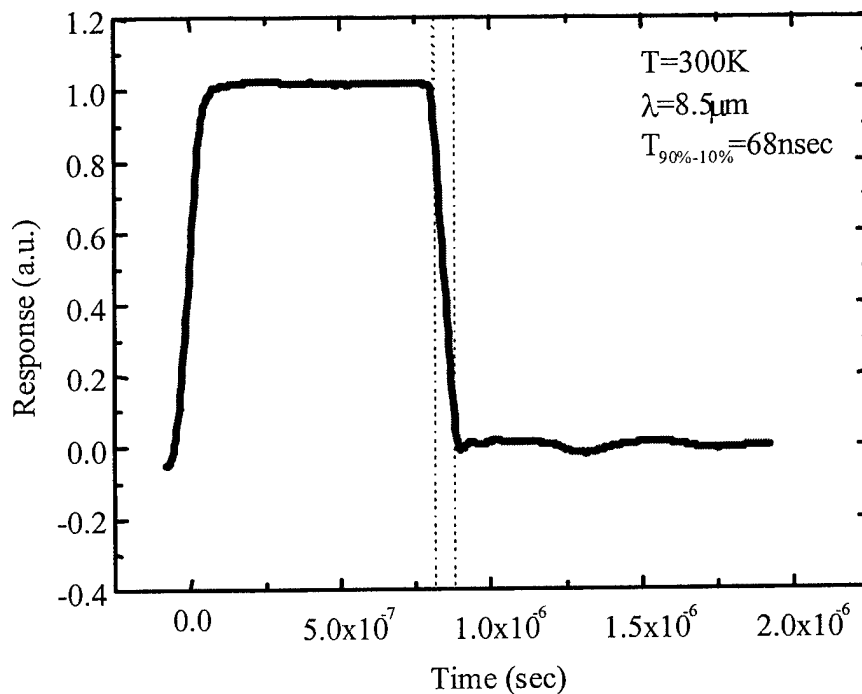


Figure 27. The overall response of the setup.

II.J. Device Performance and Comparison with State of the Art

The performance of infrared detectors is usually compared based on their detectivity which is an indication of their sensitivity. Knowing the responsivity and the noise of the devices, we could calculate their detectivity. The uncooled devices show a detectivity of about $1.3 \times 10^8 \text{ cmHz}^{1/2}/\text{W}$ at $\lambda=11\mu\text{m}$ which is higher than the detectivity of commercially available HgCdTe at similar wavelengths and temperature²⁷ (see Figure 28). Unlike HgCdTe, these Type II superlattices are grown on conventional GaAs substrates, and hence highly uniform material can be grown on three and five inch wafers readily.

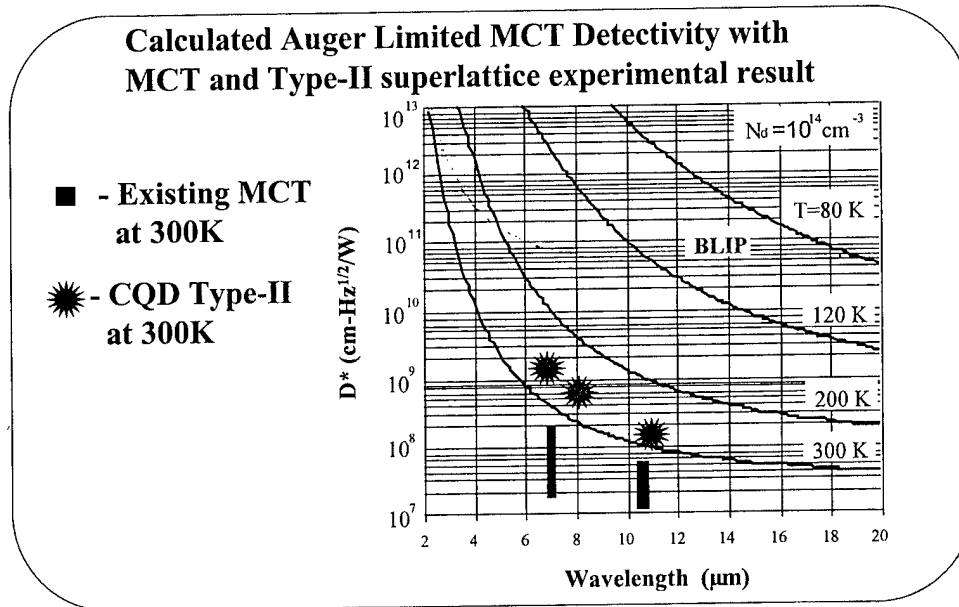


Figure 28. The detectivity of Type II superlattices compared to the theoretical limit and experimental detectivity of HgCdTe (MCT) detectors at 300 K at $\lambda \sim 11 \mu\text{m}$.

In comparison to the thermal detectors, such as microbolometers, Type II superlattices have similar detectivity, but are showing at least five orders of magnitude faster response²⁸. Although thermal detectors with higher detectivity are possible, the price that one has to pay is the speed. The change of the temperature of a bolometer is:

$$\Delta T = \frac{\eta P_0}{G \sqrt{1 + \omega^2 \tau^2}} \quad (34)$$

where ΔT is the temperature change, P_0 is the IR power that comes to the bolometer surface, η is the percentage of the IR power that is absorbed, G is the thermal conductance of the bolometer, ω is the frequency of the IR emission, and τ is the thermal response time of the bolometer and is $\tau = C/G$, where C is the thermal capacitance of the bolometer. It is easy to find that at low frequencies $\omega\tau \ll 1$, the change of the temperature is $\Delta T \sim \eta P_0/G$. Therefore, the major effort to improve the responsivity of the thermal detectors is based on the reduction of the thermal conductance, G . However, this will increase the response time of the device if one can not reduce its thermal capacitance, since $\tau = C/G$. Unfortunately, the thermal capacitance of the microbolometers cannot be reduced further since it requires a thinner or smaller device that is not practical. In order to decrease the thermal conductance of the device, the length of the legs that are supporting the sensitive layer can be increased (see Figure 29).

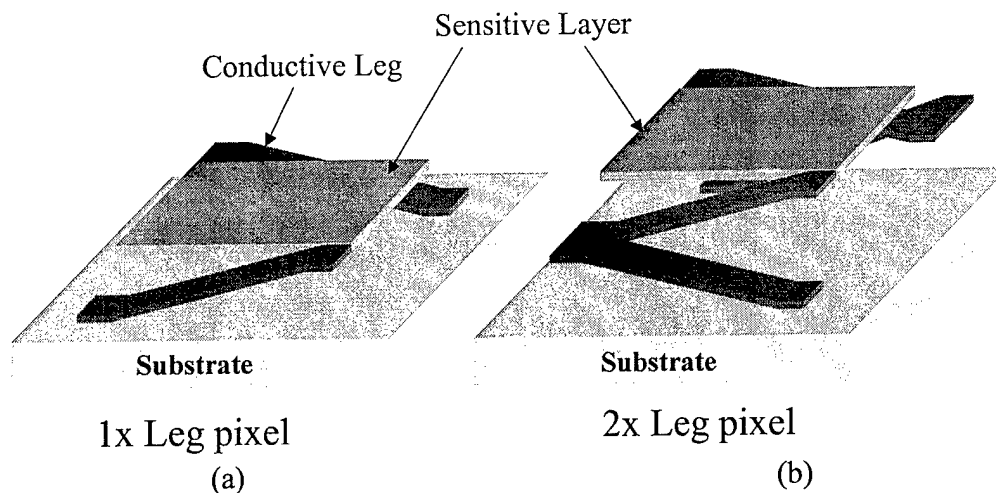


Figure 29. Schematic diagram of microbolometers with (a) original pixel legs, and (b) two times longer legs.

Figure 30 shows the relative frequency response of pixels with different leg lengths presented by Raytheon. Although increasing the leg length by a factor of four decreases the NEDT by nearly a factor of two, the 3 dB frequency knee also decreases by a factor of four²⁹.

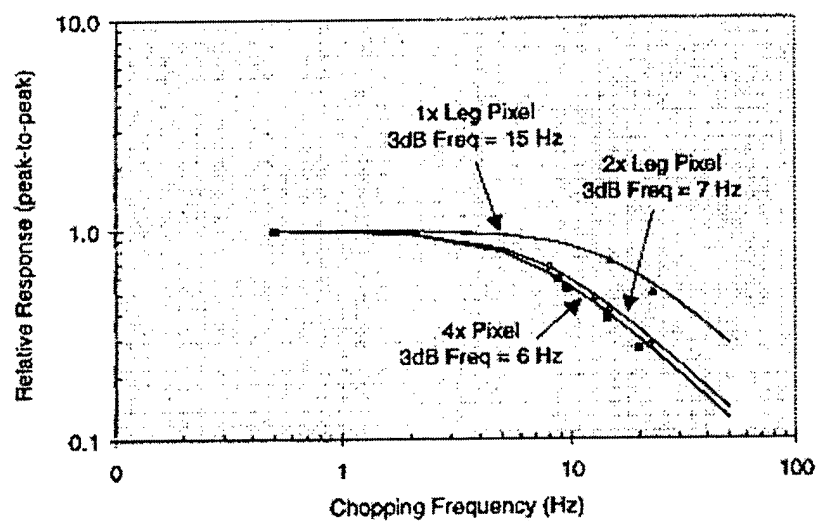


Figure 30. The relative frequency response of different test pixels with standard Raytheon Sb-151 leg length and 2 times and 4 times longer legs.

III. Realization of Uncooled Type II Photodiodes in the Long Wavelength IR (LWIR) range

III.A. Motivation

The need for uncooled photon detectors in the mid and long wavelength IR ranges as well as the limitation of currently available photon detectors have been detailed in section V.A. Although we demonstrated a high performance uncooled photoconductor in the long wavelength range based on Type II superlattices, this device is more suitable for single-element detectors and cannot be easily used for staring two-dimensional (2D) focal plane arrays (FPA). Unlike a photoconductor, the current of a photodiode flows perpendicular to the surface, and hence it is scaled by the area of the device. For example, the current of a $50\text{ }\mu\text{m} \times 50\text{ }\mu\text{m}$ photoconductor at a given voltage bias is equal to the current of a $1\text{ cm} \times 1\text{ cm}$ device, while the current of a $50\text{ }\mu\text{m} \times 50\text{ }\mu\text{m}$ photodiode is 40000 times less than the current of a $1\text{ cm} \times 1\text{ cm}$ device. This fact becomes very crucial for currently used large area FPAs, with, for example, $512 \times 512 = 262,144$ elements.

Moreover, photodiodes can operate even at zero bias which not only reduces the bias and heat dissipation requirements significantly, but also eliminates the $1/f$ noise. This type of noise increases inversely with frequency, and can be the dominant source of the total noise for low frequency applications such as IR imaging systems.

III.B. Modeling and Simulation of the Device

The active layer of these p-i-n photodiodes is a short period superlattice and hence the precise modeling of the device requires the modeling of the carrier transport in such superlattices. However, such modeling is very complex and requires massive numerical calculations³⁰. Therefore, for these superlattice-based devices, we decided to adopt the general models available for bulk semiconductors. Fortunately, the simulated results based on such modeling showed an excellent agreement with our experimental measurements. This means that the models are suitable for devices with a wide range of cutoff wavelengths (from $\sim 8\text{ }\mu\text{m}$ to $\sim 16\text{ }\mu\text{m}$) as well as operating temperatures (80 K to 300 K). The total current density of a photodiode, J_{total} , is the summation of the dark current density, J_{dark} , which is a function of the voltage bias and the photocurrent density, J_{photo} , which is a function of the bias and photon flux. We simulated photo and dark current separately, since they can be measured independently.

III.B.1. Dark Current Modeling(Voltage-Current Characteristics)

The main current components of a photodiode under no illumination (dark current) are the diffusion, the generation-recombination (GR), and the tunneling currents:

$$J_{\text{dark}} = J_{\text{Diff}} + J_{\text{GR}} + J_{\text{t}} \quad (35)$$

In the following, we develop the formalism needed for the modeling of the current density of these components.

a. Diffusion Current Density

The diffusion current is a fundamental mechanism in a p-n junction and is due to the diffusion of the minority carriers to edge of the depleted layer. The density of the diffusion current J_{Diff} is related to the voltage bias of the diode by:

$$J_{\text{Diff}} = J_s \left(e^{\frac{qV_B}{kT}} - 1 \right) \quad (36)$$

where V_B is the voltage bias, J_s is the leakage current density of the diode, q is the electron charge, k is the Boltzmann constant, and T is the absolute temperature. The leakage current density can be calculated from³¹:

$$J_s = \frac{qD_h n_i^2}{nL_h} \tanh\left(\frac{x_n}{L_h}\right) + \frac{qD_n n_i^2}{pL_n} \tanh\left(\frac{x_p}{L_n}\right) \quad (37)$$

where n and p are the electron and hole concentrations in the p-type and n-type layers respectively, D_e and D_h are their diffusion coefficients, and L_e and L_h are their diffusion lengths. x_n is the thickness of the n-type layer and x_p is the thickness of the p-type layer. n_i is the intrinsic carrier concentration and is calculated based on a three dimensional density of states approximation:

$$N_c = 2 \left\{ \frac{kTm_e}{2\pi\hbar^2} \right\}^{3/2}; N_v = 2 \left\{ \frac{kTm_h}{2\pi\hbar^2} \right\}^{3/2}; n_i = (N_c N_v)^{0.5} e^{\left(\frac{-E_g}{2kT}\right)} \quad (38)$$

where m_e and m_h are the electron and hole effective masses. E_g is the effective bandgap of the superlattices. The diffusion lengths can be extracted from the carrier mobility μ at a given temperature T , using:

$$D = \frac{kT}{q} \mu \quad (39)$$

Also, the diffusion length can be calculated from the carrier lifetime τ and the diffusion coefficient D :

$$L = \sqrt{D\tau} \quad (40)$$

b. Generation-Recombination Current Density

The generation-recombination (GR) current is due to the GR process in the depleted layer of the photodiode. Our approximation was based on a symmetric p-n junction³², since it is much simpler than the approximation for a n-p+ junction³³ while it gives similar results for our parameters:

$$J_{\text{GR}} = \frac{qn_i w(V_B)}{\tau_{\text{GR}}} \frac{2\text{sh}\left(\frac{qV_B}{2kT}\right)}{\frac{q}{kT} \left(\frac{E_g}{q} - V_B \right)} f(V_B); f(V_B) = \int_0^\infty \frac{dx}{x^2 + 2e^{(-qV_B/2kT)}x + 1} \quad (4)$$

where τ_{GR} is the GR carrier lifetime in the depleted layer. $w(V_B)$ is the thickness of the depleted layer at a voltage of V_B , and using space charge approximation it is:

$$w(V_B) = \frac{\left(\frac{E_g}{q} - V_B \right)}{E(V_B)} \quad (41)$$

where $E(V_B)$ is the electric field in the space charge region and can be approximated as:

$$E(V_B) = \left\{ \frac{2q}{\epsilon_s} \frac{np}{n+p} \left(\frac{E_g}{q} - V_B \right) \right\}^{1/2} \quad (42)$$

where ϵ_s is the permittivity of the semiconductor.

c. Tunneling Current Density

Tunneling current is due to the tunneling of the electrons from the valence band to the conduction band through the bandgap of the semiconductor. Here, the tunneling current of the detectors is approximated based on a triangular potential barrier³⁴:

$$J_t = \frac{q^3 E(V_B) V_B}{4\pi^2 \hbar^2} \left(\frac{2m_e}{E_g} \right) \exp \left(\frac{4(m_e)^{0.5} E_g^{1.5}}{3q\hbar E(V_B)} \right) \quad (43)$$

III.B.2. **Photocurrent Modeling (Quantum Efficiency)**

The density of the photocurrent of a photodiode under a photon flux density of Φ is directly related to its quantum efficiency, η :

$$J_{\text{Photo}} = \eta q \Phi \quad (44)$$

where q is the electron charge. The quantum efficiency of a p-i-n photodiode is the summation of the efficiency of the n-type layer, depleted layer, and the p-type layer:

$$\eta = \eta_n + \eta_w + \eta_p \quad (45)$$

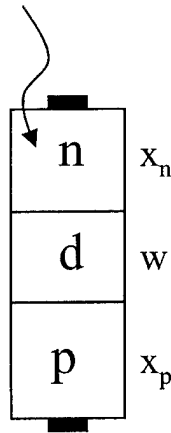


Figure 31. Schematic of a p-i-n photodiode. w is the thickness of the depleted layer, while x_n and x_p are the thickness of the undepleted n-type and p-type layers.

For our devices that are illuminated from the n-side (see Figure 31), the quantum efficiency for each of these layers can be calculated from³¹:

$$\eta_n = \frac{(1-r)\alpha L_h}{\alpha^2 L_h^2 - 1} \left\{ \frac{\alpha L_h - e^{-\alpha x_n} \sinh\left(\frac{x_n}{L_h}\right)}{\cosh\left(\frac{x_n}{L_h}\right)} - \alpha L_h e^{-\alpha x_n} \right\} \quad (46)$$

$$\eta_p = \frac{(1-r)\alpha L_e}{\alpha^2 L_e^2 - 1} e^{-\alpha(x_n+w)} \left\{ \frac{-\alpha L_e e^{-\alpha(x_p-w)} - \sinh\left(\frac{x_p-w}{L_e}\right)}{\cosh\left(\frac{x_p-w}{L_e}\right)} + \alpha L_e \right\} \quad (47)$$

$$\eta_w = (1-r) \{ e^{-\alpha x_n} - e^{-\alpha(x_n+w)} \} \quad (48)$$

where r is the surface reflectivity, α is the optical absorption coefficient, and L_e and L_h are the electron and hole diffusion lengths.

III.C. Device Design

There are two important goals in the design of an uncooled photodiode in the LWIR range. First, the differential-resistance area product (R_0A) must be high enough to reduce the thermal current noise and the dark current of the device. In fact, this has been one of the major obstacles for the realization of practical IR imaging systems based on photodiodes. Second, the quantum efficiency of the device must be high enough to have a considerable signal level.

The value of R_0A can be easily calculated from the devices' dark current density:

$$R_0A = \frac{1}{\left. \frac{\partial J_{\text{dark}}}{\partial V_B} \right|_{V_B=0}} \quad (49)$$

It is also helpful to separate the contribution of different components of the dark current to the R_0A . These are namely the diffusion related $(R_0A)_{\text{diff}}$, the GR related $(R_0A)_{\text{GR}}$, and the tunneling related $(R_0A)_t$:

$$\begin{aligned} (R_0A)_{\text{diff}} &= \frac{kT}{qJ_s}; \\ (R_0A)_{\text{GR}} &\approx \frac{V_B \tau_{\text{GR}}}{qn_i w(V_B)}; \end{aligned} \quad (50)$$

$$(R_0A)_t = \frac{h^2 \epsilon_s^{1/2}}{2m_e^{1/2} q^3 N_{\text{eff}}^{1/2}} \exp \left\{ \frac{8\pi m_e^{1/2} E_g \epsilon_s^{1/2}}{3qhN_{\text{eff}}^{1/2}} \right\};$$

where J_s , τ_{GR} , V_B , $w(V_B)$, n_i , m_e , E_g , and ϵ_s are defined in the previous section. N_{eff} is the effective doping density which is equal to $np/(n+p)$, and h is the Planck constant. Since these resistances are effectively in parallel, the overall R_0A product is:

$$\frac{1}{R_0A} = \frac{1}{(R_0A)_{diff}} + \frac{1}{(R_0A)_{GR}} + \frac{1}{(R_0A)_t} \quad (51)$$

This means that R_0A is similar to the component with the lowest value. In the case of devices with a cutoff wavelength close to $\lambda_c=8\mu m$ at room temperature, $(R_0A)_{Diff}$ is much lower than the other components, and hence is the most important parameter of the design. This parameter can only be increased by decreasing the leakage current J_s . A quick study of the formula for J_s shows that one can decrease J_s by: first decreasing mobility μ , second increasing carrier lifetime τ , and third decreasing x_n and x_p .

The mobility of the electrons and holes are naturally reduced by interface scattering in Type II superlattices and the estimated mobility is on the order of $\sim 100 \text{ cm}^2/\text{Vs}$ for electrons and ten times lower for holes³⁵. This is a definite advantage of Type II SLs since these are orders of magnitude smaller than similar values for InAsSb or HgCdTe where electron mobility is around $\mu_e \sim 100,000 \text{ cm}^2/\text{Vs}$!

In the previous chapter, we showed that the carrier lifetime τ of a properly designed Type II SL is nearly one order of magnitude longer than the carrier lifetime in a narrow gap bulk material (e.g. InAsSb and HgCdTe).

The third point indicates that x_n and x_p must be reduced. However, a glance at the formula of quantum efficiency shows that such action can also reduce the quantum efficiency of the device. The question, however, is which value of x_n and x_p is optimum in this tradeoff. Using the parameters that were extracted from the simulation of the dark current of the processed devices, I could simulate the quantum efficiency versus x_n and x_p as is shown in Figure 32. The parameters that were used are $\mu_e=100 \text{ cm}^2/\text{Vs}$, $\mu_h=10 \text{ cm}^2/\text{Vs}$, $\alpha=2000 \text{ cm}^{-1}$, $w=45 \text{ nm}$, and $\tau=20 \text{ ns}$. Figure 33 shows the calculated leakage current density J_s for the same set of parameters.

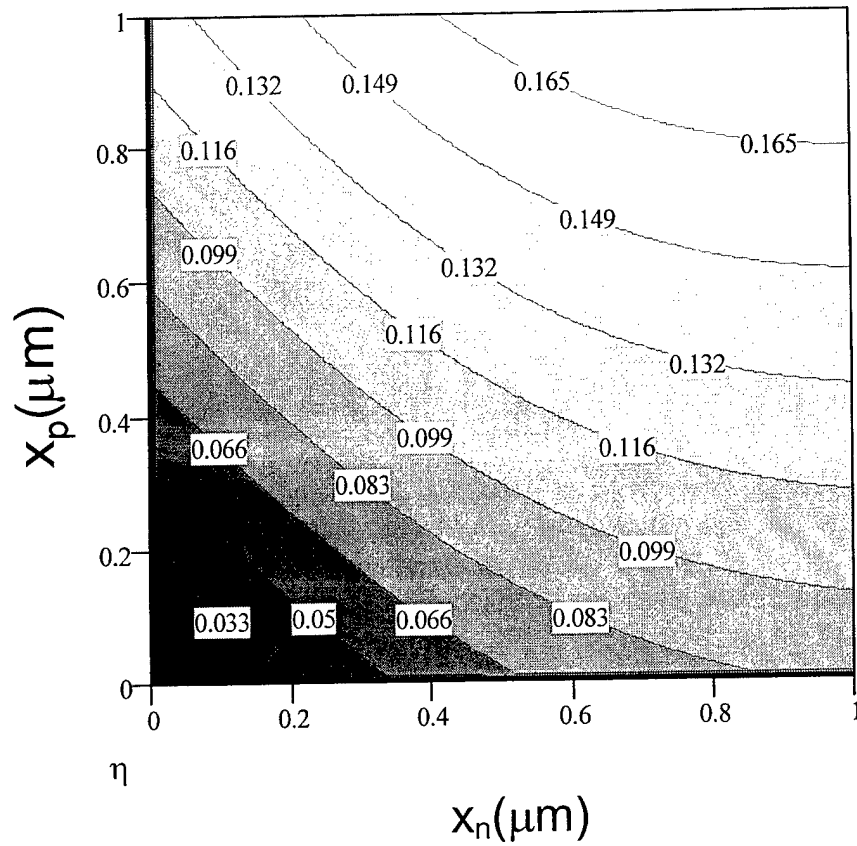


Figure 32. The calculated quantum efficiency of a device with $\lambda_c=8\mu\text{m}$ at room temperature versus the thickness of the n-type (x_n) and p-type (x_p) layers.

The value of leakage current density is clearly a more sensitive function of layer thickness. For example, J_s is nearly five times higher for $x_n=x_p=0.2\mu\text{m}$ compared to $x_n=x_p=1.0\mu\text{m}$, while η is only ~ 3.6 times higher.

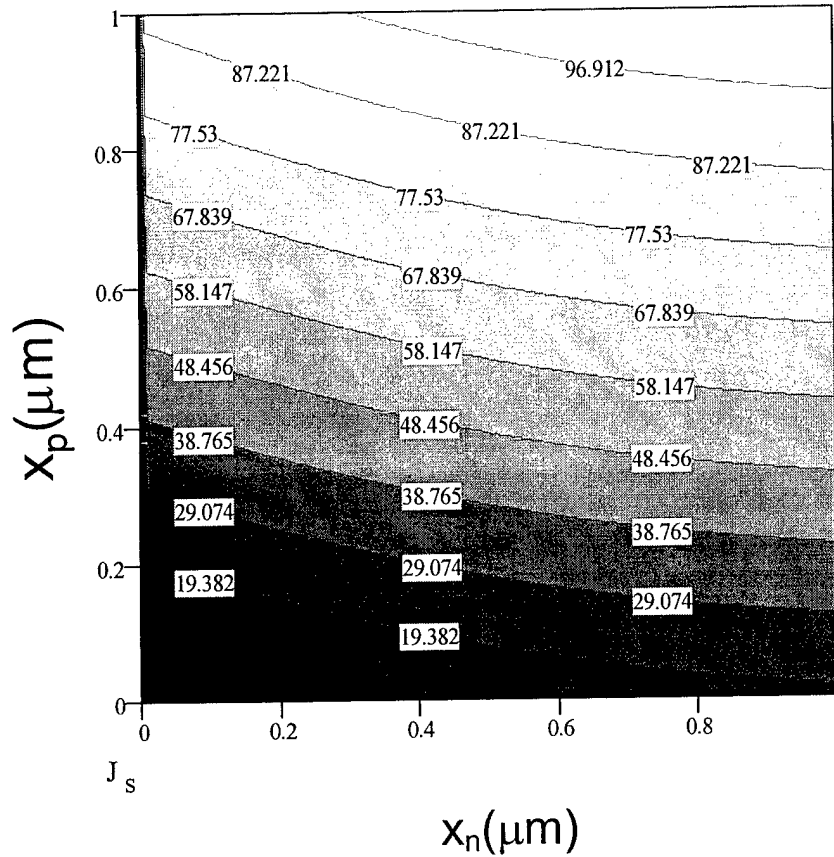


Figure 33. The calculated leakage current density (in A/cm^2) of a device with $\lambda_c=8\mu\text{m}$ at room temperature versus the thickness of the n-type (x_n) and p-type (x_p) layers.

The detectivity is proportional to quantum efficiency and the inverse square root of the leakage current density or equally to the square root of R_0A product ($J_s \propto 1/R_0A$).

Therefore, the detectivity of a device with $x_n=x_p=1.0\mu\text{m}$ is $3.5/\sqrt{5} \approx 1.56$ times higher than a device with $x_n=x_p=0.2\mu\text{m}$ while its quantum efficiency is 3.5 times higher.

So far the thicker device in this example has clear advantages: higher detectivity (56%) and higher quantum efficiency (3.5 times), while its only disadvantage is lower R_0A (5 times). However, I realized that the thickness is a very important issue which can be used to improve the performance of the device. I developed a novel design in which several p-i-n devices can be grown on top of each other and act as a series of detectors. A detailed study of this new device design, called a multiple junction detector (MJD) in this thesis, showed excellent properties compared to the conventional p-i-n design with a similar thickness. For example, an MJD consisting of five p-i-n junctions with $x_n=x_p=0.2\mu\text{m}$ have an overall thickness and growth time of the device with $x_n=x_p=1.0\mu\text{m}$. However, the MJD has $5 \times 5 = 25$ times higher R_0A and $\sqrt{25}/3.5 = 1.43$ times higher detectivity, but 3.5 times lower quantum efficiency compared to a simple p-i-n with similar thickness.

Fortunately, high quantum efficiency is not as important as high detectivity for the imaging of room temperature objects (e.g. medical thermal imaging), since the photon

flux is quite high. Good examples of high performance IR imaging arrays with only a few percent quantum efficiency are cooled Schottky barrier silicide detectors and uncooled microbolometers.

Moreover, the above values of quantum efficiencies are the so-called "internal" quantum efficiencies. The "external" quantum efficiency is the overall quantum efficiency of a system consisting of the detector and a read-out circuit. The ratio of the external to the internal quantum efficiency is equal to the ratio of the current that reaches the read-out circuit to the photo-generated current. This ratio is related to the impedance of the detector R_d and the read-out circuit R_r as:

$$\frac{\eta_{\text{external}}}{\eta_{\text{internal}}} = \frac{1}{1 + R_r / R_d} \quad (52)$$

This formula shows that external quantum efficiency approaches the internal quantum efficiency only if the resistance of the detector is much higher than the read-out circuit. In fact, the differential resistance of the bulk-based uncooled photodiodes is so low that the above situation cannot be met and external quantum efficiency is much lower than the internal values. Therefore, the MJD design of the above example with 25 times higher differential resistance can have even a higher *overall* quantum efficiency than the simple p-i-n design, depending of the impedance of the read-out circuit.

III.D. Growth

The structures were grown using cracked As and Sb sources. The cracking zone temperature for both cells was 900°C. The deposition rates of the material were calibrated with dynamic RHEED oscillation to within 1%. First, 1 μm of GaSb contact layer doped with Be ($N_A=1 \times 10^{18} \text{cm}^{-3}$) was grown on a GaSb-p substrate. Then a stack of five devices was grown, each of which consisted of 20 periods of p-type InAs/GaSb:Be (39 Å/40 Å), 20 periods of nominally undoped InAs/GaSb (39 Å/40 Å), and 20 periods of n-type InAs:Si/GaSb (39 Å/40 Å) superlattices. GaSb layers in this superlattice had a graded doping from 10^{18}cm^{-3} to $2 \times 10^{17} \text{cm}^{-3}$. In the n-type superlattice, InAs layers were doped with Si ($N_D=2 \times 10^{18} \text{cm}^{-3}$). The shutter sequences were designed such that both interfaces were InSb type. Finally, the growth was capped with a 0.01 μm InAs:Si layer ($N_D=1 \times 10^{18} \text{cm}^{-3}$). The growth temperature was about 520°C for the GaSb and 395°C for the superlattices according to a pyrometer calibrated with the surface reconstruction transition temperatures of GaSb (~390°C) and InSb (~380°C).

III.E. Structural Characterization

High resolution x-ray diffraction and atomic force microscopy (AFM) showed excellent crystal quality and surface smoothness of the samples. We could routinely grow samples with less than 0.1% mismatch to the GaSb substrates and less than 4 Å root mean square (rms) surface roughness. Figure 34 shows the rocking curve diffraction pattern of the grown material in the (004) crystal direction. High order satellites with sharp peaks indicate a uniform crystal period and excellent crystal quality and sharp interfaces.

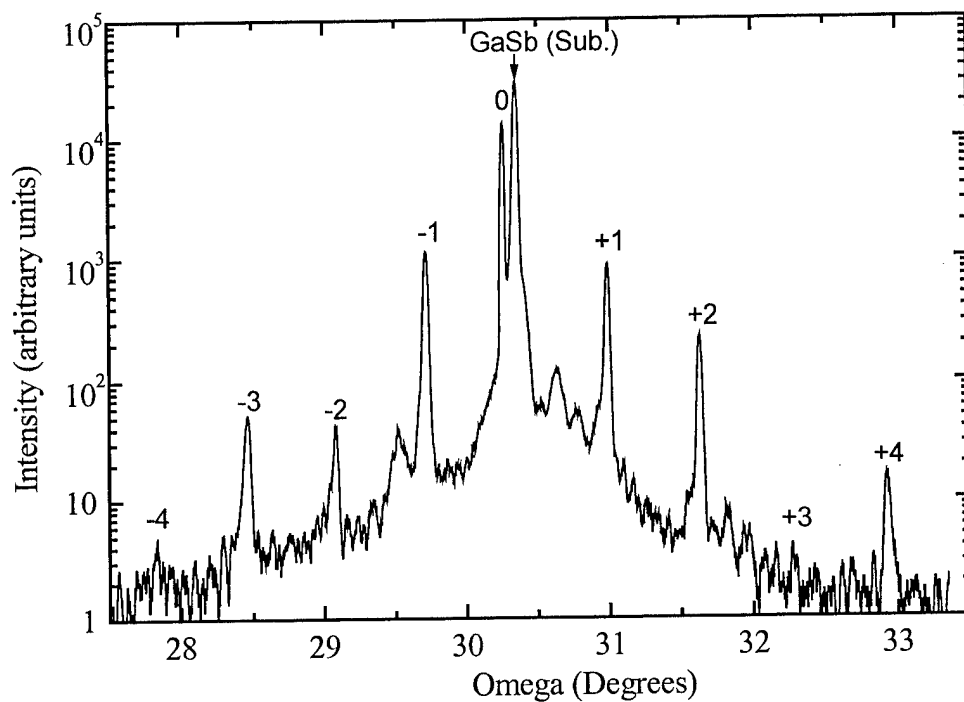


Figure 34. High resolution x-ray diffraction pattern of the grown material shows the small mismatch of the superlattice to the GaSb substrate as well as high order satellites with sharp peaks.

Figure 35 shows the atomic force microscopy (AFM) image of the surface as well as the results of a roughness analysis program. The rms surface roughness over a $20\text{ }\mu\text{m} \times 20\text{ }\mu\text{m}$ area is only $1.9\text{ }\text{\AA}$ which is the best reported value for Type II InAs/Ga_{1-x}In_xSb/InAs superlattices grown on GaSb substrates.

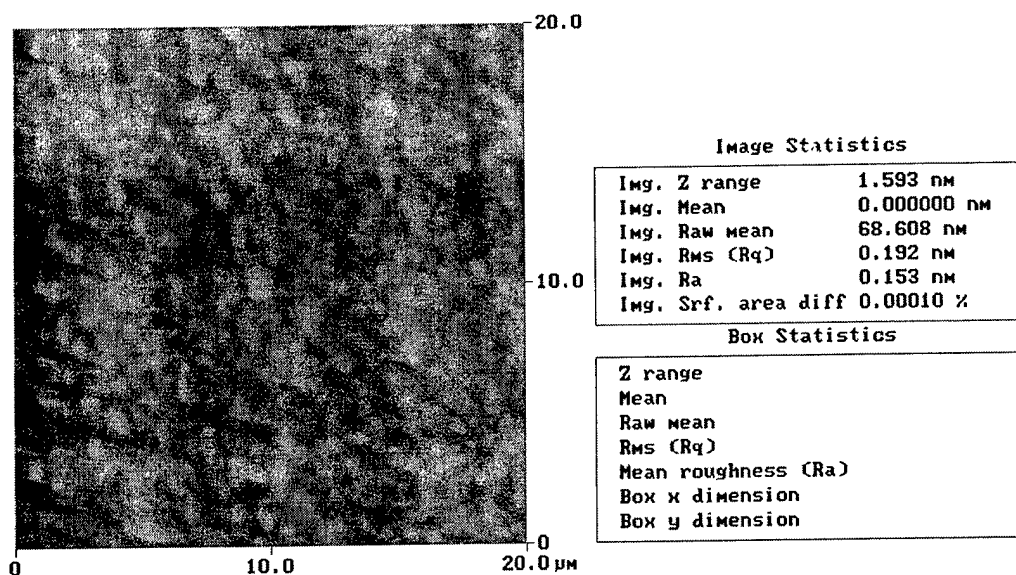


Figure 35. AFM image of the surface morphology of the sample as well as the roughness analysis. The rms surface roughness over a $20\ \mu\text{m} \times 20\ \mu\text{m}$ area is only 1.9\AA .

High resolution AFM images of the surface of the grown material show wide atomic steps (see Figure 36) which is an indication of excellent surface smoothness of the samples.

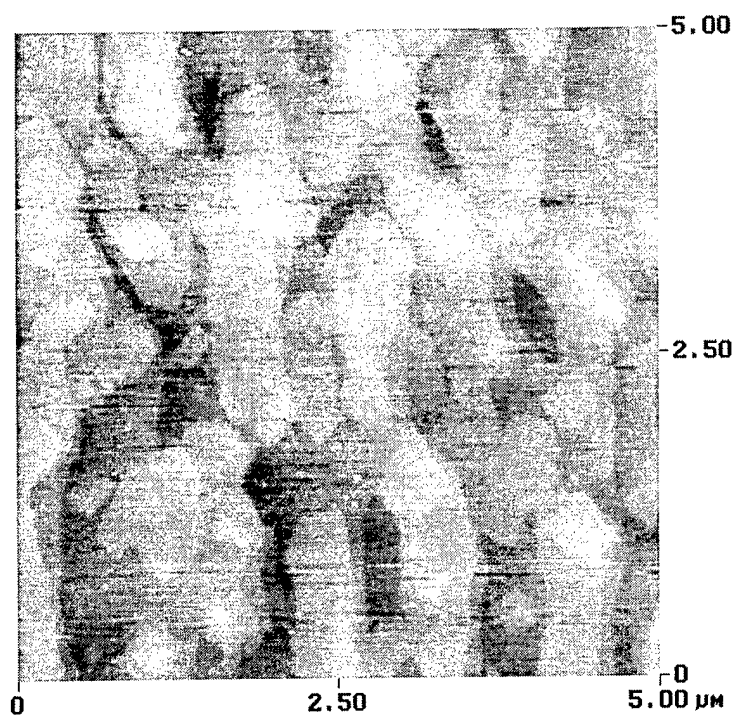


Figure 36. High resolution AFM image of the surface of the device shows atomic steps as wide as $2\text{ }\mu\text{m}$ indicating excellent surface smoothness of the grown material.

III.F. Device Processing

The samples were then processed into $400\text{ }\mu\text{m} \times 400\text{ }\mu\text{m}$ mesas using standard photolithography and a new wet etching solution. The major challenge for the development of the etching solution comes from the fact that it should etch a superlattice with three different materials: InAs, InSb, and GaSb. Although one can use a solution which only etches one material and the others will be pilled off due to the under etching effect, I realized this will not provide a controllable etching method. The only existing etching solutions that etch nearly all III-V materials with a similar rate are bromine based solutions. Unfortunately the etching mechanism is diffusion-limited, and hence the inevitable non-uniformity of the solution flow makes the etching rate and the shape of the sidewalls non-uniform. They also attack the photoresist mask, and therefore a dielectric mask (e.g. SiO_2) must be used which increases the processing complexity considerably. The solution that I developed is a mixture of citric acid, hydrogen peroxide, phosphoric acid and water (2:3:2:20). It etches all superlattice layers with a similar etching rate of $\sim 0.5\text{ }\mu\text{m}/\text{min}$ which is well in the controllable range. It has also a reaction-limited mechanism, and so the etching rate is independent of the agitation level of the solution and highly uniform mesas can be etched over a large area (see Figure 37).

For top and bottom contacts we used Ti/Au ($500\text{ }\text{\AA}$ / $1200\text{ }\text{\AA}$), defined with electron beam evaporation and lift-off techniques. No passivation or anti-reflection coating was used on the surfaces of the samples.

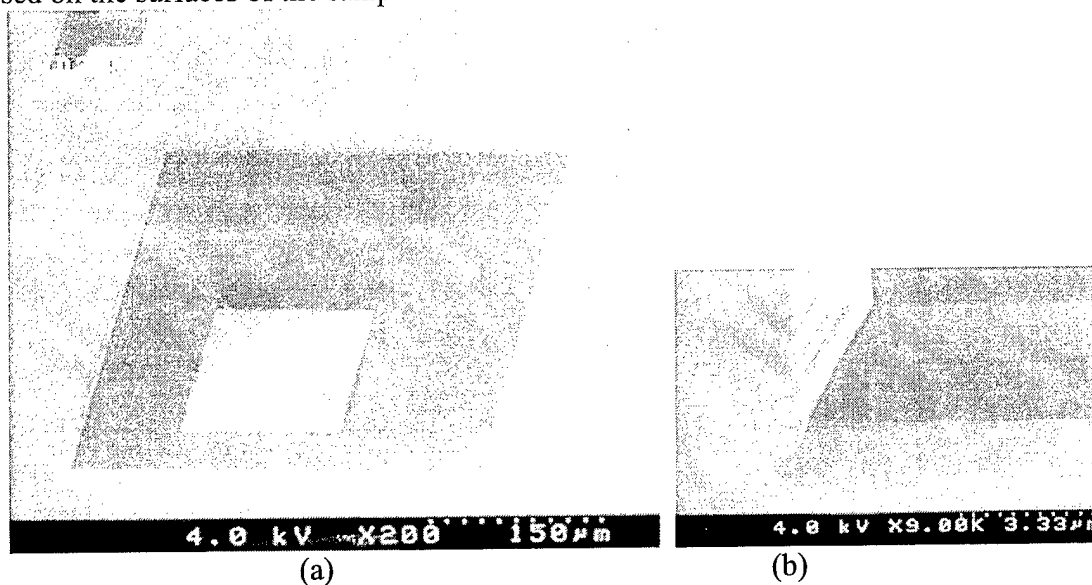


Figure 37. The SEM images of (a) a $400\text{ }\mu\text{m} \times 400\text{ }\mu\text{m}$ mesa and (b) the magnified edge of the mesa. The wet etching provides smooth beveled edges with a $\sim 60^\circ$ angle.

III.G. Device Measurement

III.G.1. Current-Voltage Characteristics

The current-voltage (I-V) characterization of the devices was measured with a HP 4155A parameter analyzer. Figure 38 shows the current density and differential resistance area product (RA) versus the bias of a device. The value of the differential resistance at zero bias is $R_0A=1.36 \times 10^{-2} \Omega\text{cm}^2$ which is more than two orders of magnitude higher than $R_0A \sim 10^{-4} \Omega\text{cm}^2$ of HgCdTe detectors with a similar bandgap at room temperature³⁶.

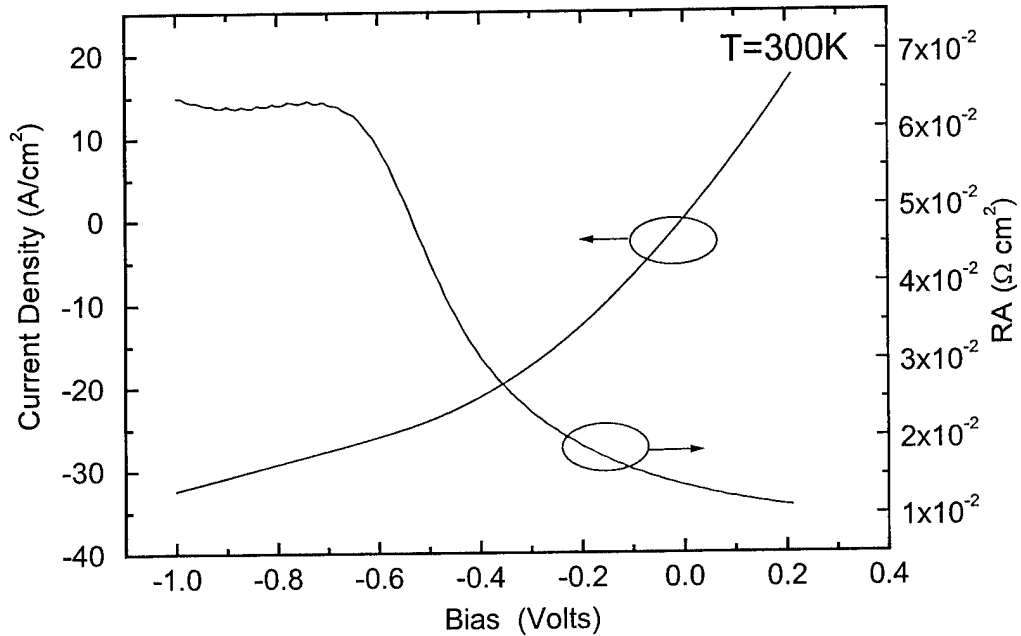


Figure 38. The current density and differential resistance area product (RA) of a device versus the voltage bias.

Figure 39 compares the calculated current density of a device and the measured values. Current density simulation uses the formalism given in VI.B.1 and shows excellent agreement to the experimental data. The fit parameters are only the carrier lifetime $\tau_e=\tau_h=20$ nsec, and $\tau_{GR}=0.6$ nsec. We used $\mu_e=100\text{cm}^2/\text{Vs}$ and $\mu_h=10\text{cm}^2/\text{Vs}$ which were extracted from the experimental results in $\text{Ga}_{1-x}\text{In}_x\text{Sb}/\text{InAs}$ superlattices with a similar.

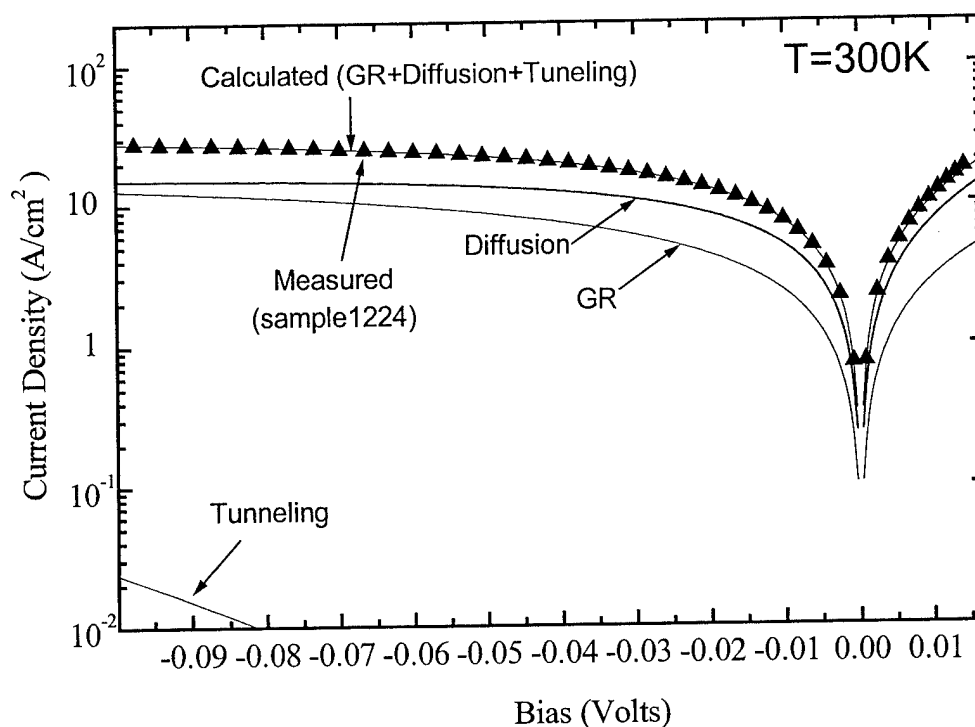


Figure 39. The calculated current density versus the voltage bias compared to the measured values for sample SSMBE 1224 at $T=300\text{K}$ shows excellent agreement in reverse and forward biases.

III.G.2. Optical Responsivity

Absolute spectral responsivity was calculated from the measured spectral response of the devices, using a Fourier transform infrared (FTIR) spectroscopy system, and the device's photoresponse to a calibrated blackbody setup. The peak responsivity was $R_i=0.14 \text{ A/W}$ at $\lambda=7 \mu\text{m}$ leading to a Johnson noise limited detectivity of $D^*=1.2 \times 10^8 \text{ cmHz}^{1/2}/\text{W}$ at room temperature. Figure 40 shows the detectivity of a device versus IR wavelength and energy. Although the IR path length in the atmosphere was only about 15 cm, CO_2 and water vapor absorption features are visible in the spectrum.

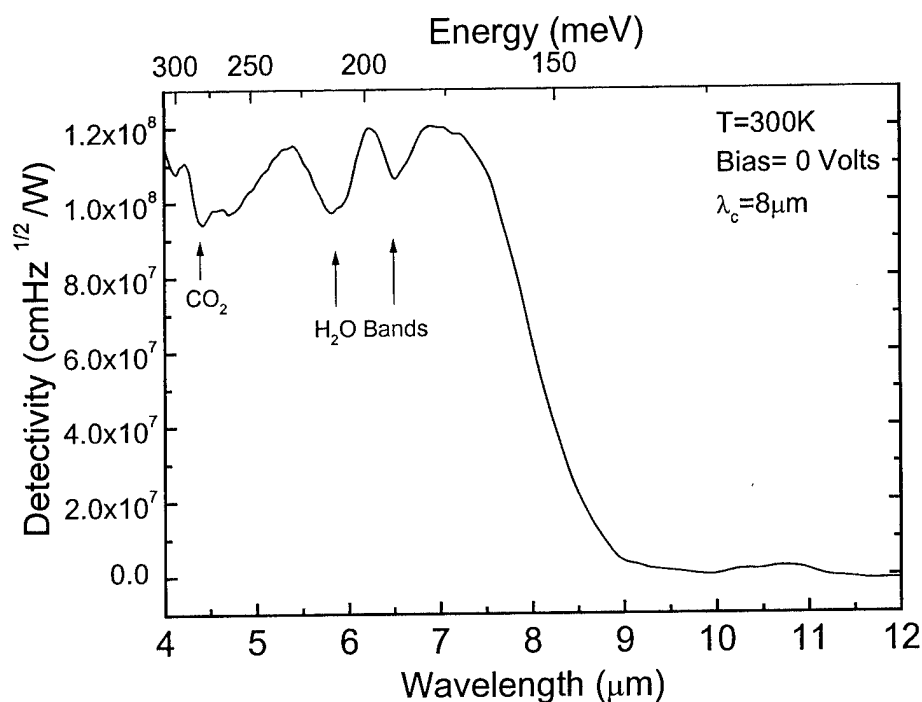


Figure 40. The Detectivity of a device versus the wavelength and energy of the IR radiation. Features at 4.3 μm and 6-7 μm are due to the CO_2 and water vapor absorption during the measurement.

III.G.3. Noise Measurement

Although non-equilibrium HgCdTe and InAsSb detectors with high differential resistance under reverse bias have been demonstrated recently³⁷, a high $1/f$ noise degrades the performance of these devices below several megahertz by two to three orders of magnitude. Consequently, these non-equilibrium devices cannot be used for low frequency applications such as IR imaging systems³⁸.

The operation of Type II photodiodes under zero bias ensures that the main noise component is the thermal (Johnson) noise and $1/f$ noise is eliminated. Our experimental measurements indicate that even under a considerable reverse bias, Type II detectors do not have a high frequency $1/f$ noise. Figure 41 shows the frequency spectrum of the amplified output of a detector. The device was under a -0.2 volt bias and illuminated by the chopped IR radiation of a blackbody. The chopper frequency was $f_0=396\text{Hz}$, blackbody temperature and aperture diameter were $T_{\text{BB}}=800\text{ K}$ and $D_{\text{BB}}=2.54\text{ cm}$, and the detector was located $d=15\text{ cm}$ away from the blackbody aperture. Although the measurement includes the noise of the pre-amplifier (Analog Device AD797) and the FFT spectrum analyzer (Stanford Research System SR 760), the knee of the $1/f$ noise is below $\sim 100\text{Hz}$. Under the given parameters of the inset of the Figure 41, the signal to

noise ratio (SNR) was more than 44dB with a bandwidth of $\Delta f=100$ Hz around $f_0=396$ Hz.

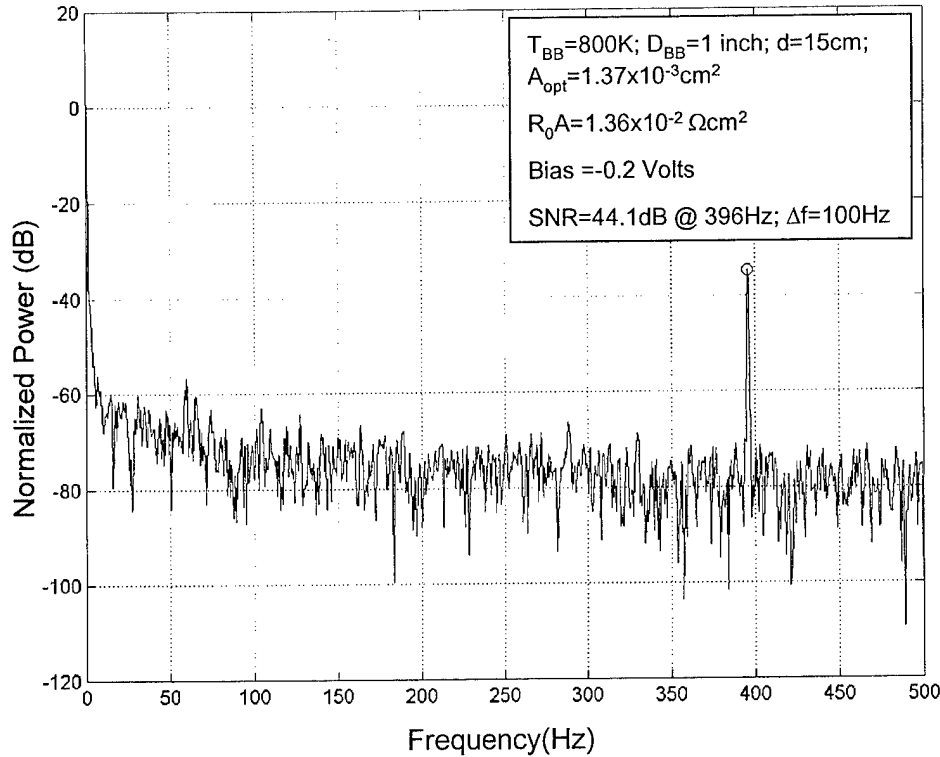


Figure 41. Frequency spectrum of the amplified output of a detector illuminated by a chopped IR radiation of a blackbody. The detector was biased at -0.2 V and was located $d=15$ cm away from the blackbody aperture.

III.G.4. Response Time

We used a quantum cascade laser (QCL), operating at room temperature³⁹, as a high-speed source of IR radiation at $\lambda=5\mu\text{m}$ to study the response time of the uncooled Type II devices. Figure 42 shows the current of the QCL as well as the output of the pre-amplifier versus time. The inset shows the schematic diagram of the measurement setup. The laser threshold current marks the current above which the laser starts emitting. Considering the fall time of the pre-amplifier (~ 50 ns) and the fall time of the output signal of the pre-amplifier (~ 110 ns), the detector response time was about $(110^2 + 50^2)^{1/2} \sim 100$ ns using the sum-of-squares approach.

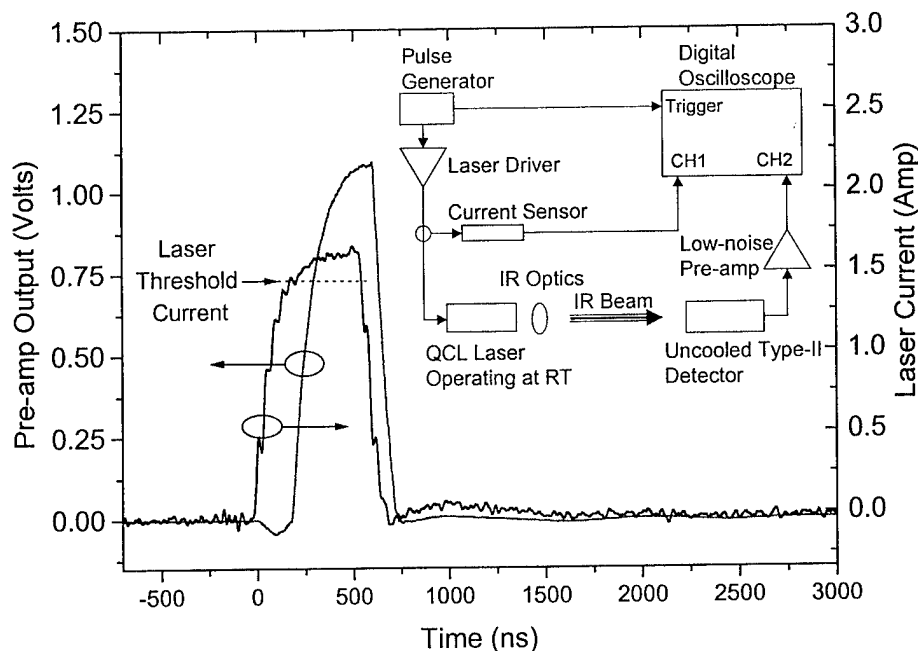


Figure 42. The current of the QCL laser (right axis) and the amplified output of the detector (left axis) versus time. Inset shows the measurement setup. Note that the laser emits when current is above the threshold level.

III.H. Device Performance and Comparison with State of the Art

The performance of state-of-the-art uncooled HgCdTe and microbolometers were detailed in V.I. We demonstrated uncooled detectors based on Type II superlattices with a 50% cutoff wavelength of $8\text{ }\mu\text{m}$. The detectivity of the devices with zero bias and without optical lenses or anti-reflection coatings was $1.2 \times 10^8\text{ cmHz}^{1/2}/\text{W}$. The response time of the detectors, measured with a quantum cascade laser at room temperature, was about 100 nsec. The following table compares the performance of these devices with available HgCdTe and microbolometer detectors.

| Parameters | Type II SL | HgCdTe | Microbolometer |
|--|---|---|---|
| Detectivity $\lambda_c=8\mu\text{m}; T=300\text{K}$ | $\sim 10^8 \text{ cmHz}^{1/2}/\text{W}$ | $\sim 10^8 \text{ cmHz}^{1/2}/\text{W}$ | $\sim 10^8 \text{ cmHz}^{1/2}/\text{W}$ |
| R_0A $\lambda_c=8\mu\text{m}; T=300\text{K}$ | $1.4 \times 10^{-2} \Omega\text{cm}^2$ | $\sim 1 \times 10^{-4} \Omega\text{cm}^2$ | ----- |
| Uniformity | Very Good | Poor | Very Good |
| Zero Bias Operation | Possible | Possible | Not Possible |
| Response Time | $\sim 10^{-8}$ second | $\sim 10^{-8}$ second | $\sim 10^{-3}$ second |

Table II. The performance of uncooled Type II superlattice photodiodes compared with the uncooled HgCdTe and microbolometer at 8 μm .

- ¹ C. H. Grein, P. M. Young, H. Ehrenreich and T.C. McGill, J. of Electronic Material **22**, 1093, (1993).
- ² H. Mohseni, V.I. Litvinov, and M. Razeghi, Phys.Rev. B **58**, 378, (1998).
- ³ D. L. Smith, T. C. McGill, and J. N. Schulman, Appl. Phys. Lett. **43**, 180, (1983).
- ⁴ C. Mailhot, D. L. Smith, J. Vac. Sci. Technol. **A7**(2), 445, (1989).
- ⁵ C.G. Van de Walle and R. M. Martin, Phys. Rev. B **35**, 8154, (1987).
- ⁶ C.G. Van de Walle, Phys. Rev. B **39**, 1871, (1989).
- ⁷ H. Mohseni, and M. Razeghi, Electrochemical Soc. Proc. **98-21**, 171 (1998).
- ⁸ H. Mohseni, J. Wojkowski, A. Tahraoui, M. Razeghi, G. Brown, and W. Mitchel, SPIE **3948**, 153, (2000).
- ⁹ Simplified LCAO Method for the Periodic Potential Problem, J. C. Slater AND G. F. Koster, Physical Review, Volume 94, Number 6, June 15, 1954
- ¹⁰ Solid State Physics, Neil W. Ashcroft, N. David Mermin, ISBN 0-03-083993-9(College Edition) pp 176-190
- ¹¹ On the Non-Orthogonality Problem Connected with the Use of Atomic Wave Functions in the Theory of Molecules and Crystals, PER-OLOV LOWDIN, The Journal of Chemical Physics, Volume 18, Number 3, March, 1950
- ¹² Efficient *ab initio* tight binding, Andrew P. Horsfield, Physical Review B, Vol 56, No 11, 15 Sept 1997
- ¹³ A SEMI-EMPIRICAL TIGHT-BINDING THEORY OF THE ELECTRONIC STRUCTURE OF SEMICONDUCTORS, P. Vogl *et al.* J. Phys. Chem. Solids Vol. 44, No. 5, pp. 365-378, 1983
- ¹⁴ Improved fits of the effective masses at Γ in the spin-orbit, second-nearest-neighbor sp^3s^* model: Results from analytic expressions, Phys. Rev. B Vol. 56, No. 15, 15 October 1997
- ¹⁵ Empirical sp^3s^* tight-binding calculation for cubic semiconductors: General method and material parameters, Jean-Marc Jancu et al, Phys. Rev. B Vol. 57, No. 11, 15 March 1998
- ¹⁶ Comparative study of band-structure calculations for type-II InAs/ $\text{In}_x\text{Ga}_{1-x}\text{Sb}$ strained-layer superlattices, D. N. Talwar and John P. Loehr, B. Jogai, Phys. Rev. B Vol. 49, No. 15, 15 April 1999

- ¹⁷ Calculated electronic structure of GaAs/Ge₂(001) superlattices, J. Rufinus and G. E. Crook, J. Appl. Phys. 81(2), 15 January 1997
- ¹⁸ Theory of electronic and optical properties of bulk AlSb and InAs and InAs/AlSb superlattices, G. Theodorou and G. Tsegas, Phys. Rev. B Vol. 61, No. 16, 15 April 2000
- ¹⁹ H. Mohseni, A. Tahraoui, J. Wojkowski, M. Razeghi, W. Mitchel and A. Saxler, SPIE **3948**, 145, (2000).
- ²⁰ N. Herres, F. Fuchs, J. Schmitz, K. Pavlov, J. Wagner, J. Ralston, P. Koidl, C. Gadaleta, G. Scamarcio, Phys. Rev. B. **53**, 15688 (1996).
- ²¹ H. Mohseni, E. Michel, J. Sandven, M. Razeghi, W. Mitchel, and G. Brown, Appl. Phys. Lett. **71**, 1403 (1997).
- ²² H. Mohseni, E. J. Michel, M. Razeghi, W. C. Mitchel, G. J. Brown, SPIE **3287**, 30 (1998).
- ²³ G. Zegrya and A. Andreev, Appl. Phys. Lett. **67**, 2681, (1995).
- ²⁴ J. Piotrowski, W. Galus, and M. Grudzien, Infrared Phys. **31**, 1, (1990).
- ²⁵ D. Wang, G. Bosman, Y. Wang, S. Li, J. Appl. Phys. **77**, 1107, (1995).
- ²⁶ S. Slivken, A. Matlis, C. Jelen, A. Rybaltowski, J. Diaz, and M. Razeghi, Appl. Phys. Lett. **74**, 173 (1999).
- ²⁷ H. Mohseni, J. Wojkowski, M. Razeghi, IEEE J. Of Quantum Elect. **35**, 1041 (1999).
- ²⁸ H. Mohseni and M. Razeghi, Proceedings 1999-ISDRS, 563 (1999).
- ²⁹ W. Radford, D. Murphy, A. Finch, K. Hay, A. Kennedy, M. Ray, A. Sayed, J. Wyles, R. Wyles, and J. Varesi, SPIE proceeding **3698**, 119 (1999).
- ³⁰ N. Einspruch and W. Frensley, Heterostructures and Quantum Devices, p. 273, Academic Press, CA, (1994).
- ³¹ H. Hovel, Semiconductors and Semimetals vol. 11 , edited by R. Willardson and A. Berr, Academic Press, New York, (1975).
- ³² C. Sah, R. Noyce, and W. Shockley, *Proc. IRE* **45**, 1228, (1957).
- ³³ S. Choo, Solid-State Elect. **11**, 1069, (1968).
- ³⁴ S. Sze, *Physics of Semiconductor Devices*, J. Wiley, New York (1981).
- ³⁵ J. L. Johnson, L. A. Samoska, A. C. Gossard, J. Merz, M. D. Jack, G. R. Chapman, B. A. Baumgratz, K. Kosai, S. M. Johnson, J. Appl. Phys. **80**, 1116, (1996).
- ³⁶ A. Rogalski and R. Ciupa, J. Appl. Phys. **77**, 3505 (1995).
- ³⁷ C. Elliott, N. Gordon, D. Wilson, C. Jones, C. Maxey, N. Metclafe, and A. Best, J. of Modern Opt. **45**, 1601, (1998).
- ³⁸ C. Elliott, N. Gordon, R. Hall, T. Phillips, C. Jones, A. Best, J. of Elec. Mater. **26**, 643, (1997).
- ³⁹ S. Slivken, A. Matlis, C. Jelen, A. Rybaltowski, J. Diaz, and M. Razeghi, Appl. Phys. Lett. **74**, 173, (1999).